Available online at www.sciencedirect.com
SCIENCE DIRECT
Journal of Asian Earth Sciences 27 (2006) 465–502
Journal of Asian Earth Sciences
www.elsevier.com/locate/jaes

Petrological and geochemical study of the Late Cretaceous ophiolite of Khoy (NW Iran), and related geological formations

Morteza Khalatbari-Jafari[a,b], Thierry Juteau[b,*], Joseph Cotten[b]

[a]Geological Survey of Iran, Tehran, Iran
[b]IUEM and UMR 6538 "Domaines océaniques", Université de Bretagne Occidentale, 29280 Plouzané Cedex, France

Received 25 February 2004; revised 28 April 2005; accepted 16 May 2005

Abstract

This paper, based on 113 new whole rock analyses and about 3500 electron microprobe analyses of the mineral phases, is dedicated to the petrography and geochemistry of the Khoy ophiolites and related formations, NW Iran. It is complementary to a previous paper published in this Journal, where we gave a detailed description of the geology of the Khoy area, including various geological field sections, two geological maps in colour, new micropaleontological data and 27 new ^{40}K–^{40}Ar datings (Khalatbari-Jafari, M., Juteau, T., Bellon, H., Whitechurch, H., Cotten, J., Emami, H., 2004. New geological, geochronological and geochemical investigations on the Khoy ophiolites and related formations, NW Iran. J. Asian Earth Sci. 23, 507–535). Our conclusions are: (a) The petrographic study confirms the field data showing the existence of two ophiolite complexes in the region of Khoy. (b) The Late Cretaceous ophiolitic lavas of the Khoy region exhibit very homogeneous T-MORB-type multi-element plots, suggesting that they were formed at oceanic spreading centers, by partial melting of a depleted mantle source, probably contaminated by one or several regional mantle plumes, responsible for their moderate enrichment in LREE. They do not show any negative anomaly for Nb, Zr or Ti, which allows us to exclude a genesis in a 'supra-subduction' environment. (c) The Late Cretaceous ophiolite of Khoy was created at a slow-spreading oceanic ridge. (d) Cryptic variations along extrusive and layered gabbros sections suggest frequent replenishment and magma mixing events in the magma chambers. (e) The 'supra-ophiolitic turbiditic series' overlying the Late Cretaceous ophiolite was accumulated in a subduction trench running along the northwestern margin of the Iran Block. This trench was fed with detrital volcanic fragments from both sides: T-MORB basalt fragments from the ocean-side, and arc-type basalts from the continent-side. (f) The meta-ophiolites of Khoy probably also represent slow-spreading conditions, and the porphyroclastic to mylonitic tectonites preserved in these metamorphic slices attest to extreme conditions of ductile shearing, characteristic of oceanic fracture zones.

Keywords: Ophiolites; Tethys; Iran; Khoy; Trace element patterns; Cryptic variations; Electron microprobe analyses

1. Introduction

In a previous paper (Khalatbari-Jafari et al., 2004), we gave a detailed geological description of the region of Khoy, located in the northwestern part of the iranian Azerbaidjan province (Fig. 1). The Khoy area exposes five main geological units, grossly forming NW–SE stripes (Fig. 2). From northwest to southwest: (1) the southern continental margin of the Central Iranian Block; (2) an 'eastern metamorphic complex', including an old meta-ophiolitic complex; (3) a supra-ophiolitic turbiditic and volcanic-sedimentary zone of Late Cretaceous–Early Paleocene age; (4) the non-metamorphic, Late Cretaceous ophiolite of Khoy; (5) a 'western metamorphic complex', representing probably a fragment of the Arabian shield.

Our main conclusion was that there are not one, but two ophiolitic complexes in the Khoy area (Fig. 2):

(1) to the east, and outcropping along the western margin of the Central Iran Block, an *older, polymetamorphic*

* Corresponding author. Address: Domaine d'Orio, rue Orio, 64700 Hendaye, France. Tel.: +33 5 5948 1634.
E-mail address: juteau@wanadoo.fr (T. Juteau).

1367-9120/$ - see front matter © 2005 Elsevier Ltd. All rights reserved.
doi:10.1016/j.jseaes.2005.05.006

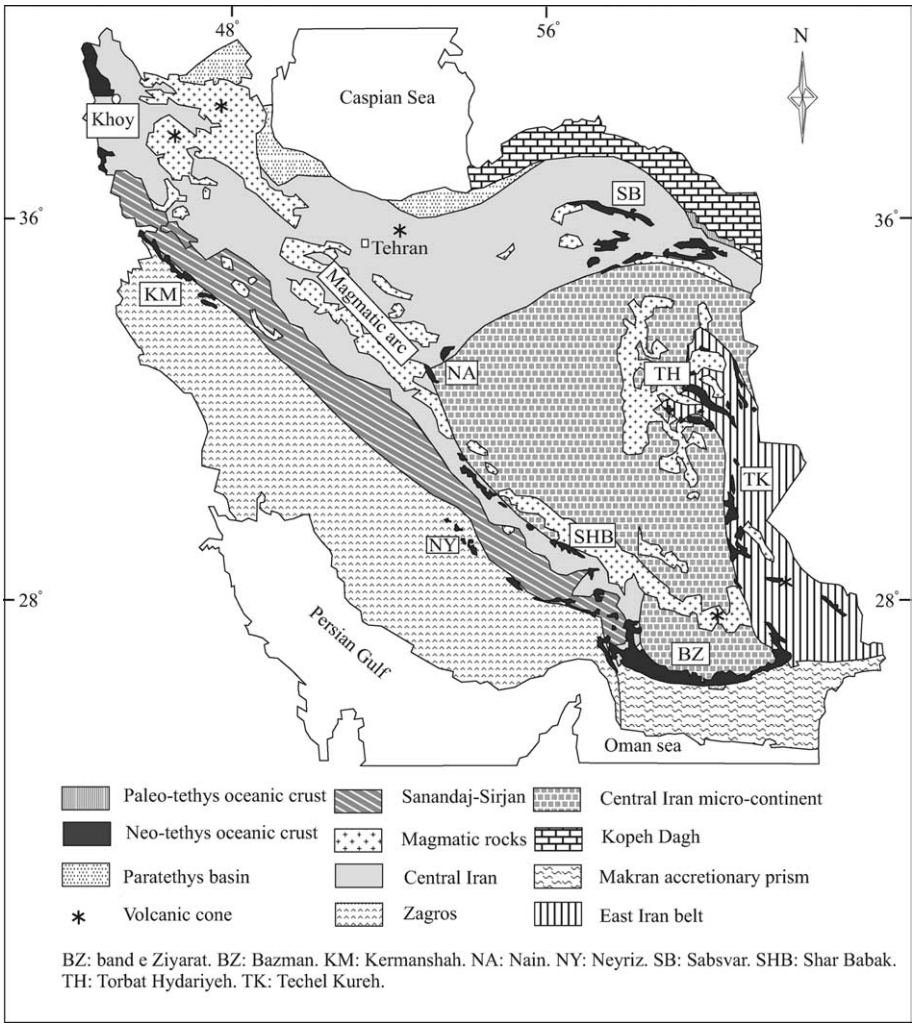

Fig. 1. Location of the ophiolites of Khoy with respect to the main ophiolite belts in Iran (in black), and to the main geological formations of Iran. Adapted from the 'Magmatic Map of Iran' at 1/1,000,000, compiled by M.E. Emami, M. Mir Mohammad Sadegi and S.J. Omrani (1993, Geological Survey of Iran) (Emami et al., 1993), and from the 'Sedimentary-structural map of Iran' by A. Aghanabati (2004).

ophiolite, tectonically included within a metamorphic subduction complex of Mesozoic age, whose oldest metamorphic amphiboles yield an Early Jurassic ^{40}K–^{40}Ar age, and whose primary magmatic age should logically be pre-Jurassic;

(2) to the west, a *younger non metamorphic ophiolite* of Late Cretaceous age, overlain by a supra-ophiolitic turbiditic, flysh-like volcanogenic series of Late Cretaceous–Early Paleocene age. This latter ophiolite was created at a slow-spreading oceanic center, as evidenced by the lherzolitic composition of the mantle sequence, the small volume of gabbroic rocks, the absence of a diabasic sheeted-dike complex, and the abundant phyric basalts in the extrusive sequence.

This paper presents the petrographic description and geochemical data concerning (a) the Late Cretaceous ophiolite of Khoy, (b) the lavas reworked in the turbiditic, supra-ophiolitic series, and (c) the metamorphic rocks of the metamorphic subduction complex, including its meta-ophiolitic slices.

1.1. Analytical techniques

One hundred and thirteen whole rock analyses for major and trace elements were performed by inductively coupled plasma atomic emission spectrometry (ICP-AES, Jobin and Yvon, analyst: J. Cotten) at the Université de Bretagne Occidentale, Brest, France.

Rock powders were dissolved into solution in closed flasks by acid attack (HF and HNO_3), and redissolution by an aqueous solution of boric acid. This method allows the rapid analysis of major elements on the simultaneous spectrometer with good reproductibility, using boron as an internal standard, and determination of 22 trace elements on the sequential spectrometer. The detection limits are

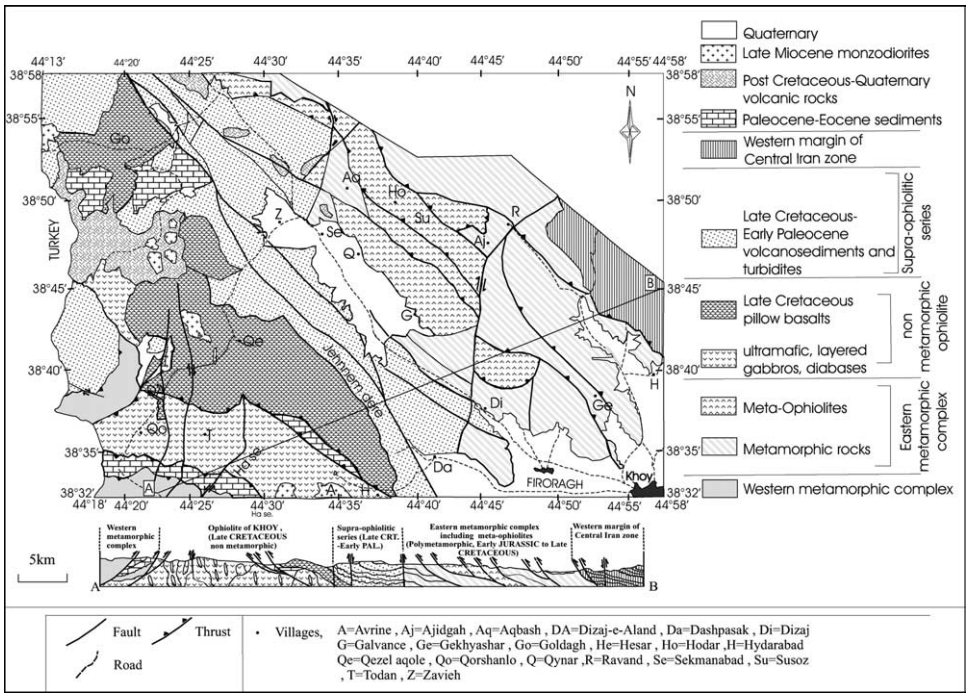

Fig. 2. Simplified geological map of the region of Khoy, and synthetic geological section, after Khalabari-Jafari (1982), and Khalabari-Jafari et al. (2003, 2004).

discussed in Cotten et al. (1995). In addition, Rb contents were determined by AAS.

Primary and secondary mineral phases were analyzed for major and minor elements on polished thin sections by electron microprobe at the 'Microsonde électronique de l'ouest' (Centre Ifremer de Brest, France), with a Camebax SX-50.

1.2. Location of the samples

The collection sites of all analyzed samples are indicated on the sketch-map of Fig. 3. In addition, sample locations are given along the various synthetic geological sections shown in Figs. 4, 6, 7 and 15.

2. The Late Cretaceous ophiolite of Khoy: petrographic study and geochemistry

The non-metamorphic, Late Cretaceous ophiolite of Khoy is composed of a *plutonic sequence*, overlain by a *thick extrusive sequence*, without an intermediary diabase sheeted dike complex.

The plutonic sequence is composed of two main petrographic units:

(1) a *mantle unit*, essentially made of serpentinized lherzolites and harzburgites;
(2) a *gabbroic unit*, forming small intrusive bodies inside the mantle unit, and generally well layered, with a wide spectrum of petrographic facies (layered wehrlites, olivine gabbros, leucocratic gabbros, anorthosites, and ferrogabbros). These rocks are crosscut by pyroxenite and isotropic gabbro veins, lobate wherlitic intrusions, and late diabase dikes.

2.1. Plutonic sequence: the mantle unit (lherzolites, harzburgites)

These rocks are extremely serpentinized. Relics of primary phases are scattered and consist of coarse olivine and orthopyroxene porphyroclasts, fine clinopyroxene crystals, and coarse to fine accessory Cr-spinels. Olivine is deeply serpentinized to lizardite and chrysotile, orthopyroxene is transformed to bastite pseudomorphs, and the Cr-spinel is oxidized to maghemite and other iron oxides-hydroxides. Only the clinopyroxene has resisted hydration and remains generally unaltered. Evidence of high-temperature deformations is difficult to observe. However, the orthopyroxene crystals are commonly stretched and sometimes bent with rolling extinctions. Olivine residues show kink-bands, and alignments of tiny recrystallized Cr-spinels may indicate the trace of a fossil foliation plane. In some thin sections, poikilitic orthopyroxene and clinopyroxene crystals surrounding rounded olivine crystals suggest the presence of impregnation zones.

Olivine compositions are very homogeneous (Fo 90–91 in average), showing typical residual mantle compositions. There are no significant chemical differences between margins and cores of the olivine crystals. The coarse clinopyroxene crystals (porphyroclasts) have an average

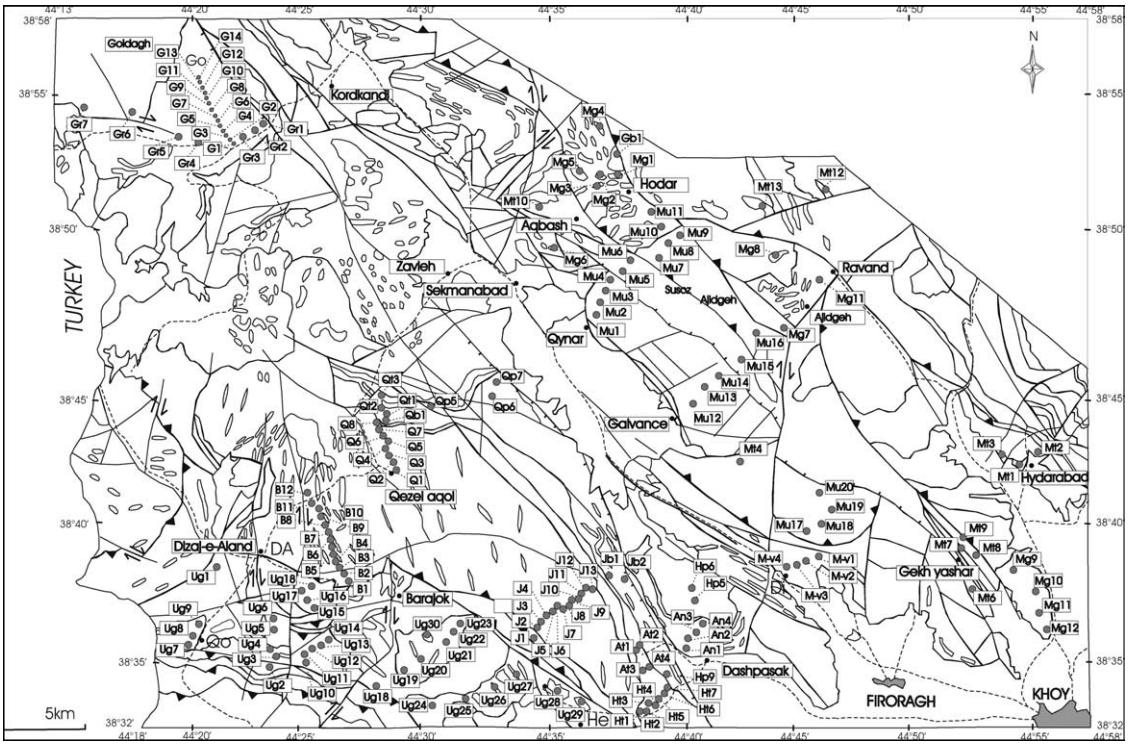

Fig. 3. Location of all analyzed rock samples. Geological contours from Khalatbari-Jafari et al. (2004, Fig. 3).

diopsidic composition (Wo48Fr3En49). The fine, recrystallized clinopyroxene crystals have practically the same average composition (Wo47Fr4En49). The orthopyroxene porphyroclasts have an average enstatite composition, without significant compositional variations between core (Wo3Fr8En89) and margins (Wo2Fr9En89). The medium-size and tiny recrystallized orthopyroxenes also have enstatite compositions (Wo2Fr9En89). The coarse Cr-spinel porphyroclasts are chemically homogeneous and contain 40–50% Cr_2O_3.

2.2. Plutonic sequence: the layered gabbro intrusive bodies

Layered gabbros occur typically as small intrusive bodies inside the peridotites (Fig. 4). They exhibit splendid magmatic layering structures and cover a wide range of facies, ranging from olivine gabbros and troctolites to pyroxene gabbros, anorthosites and ferrogabbros. On the outcrops, typical magmatic features such as lense-shaped layers, viscous folds and slumps, mineral-graded layers and compaction faults are commonly observed (Boudier et al., 1996). In several places they are intruded by wehrlitic sills and dikes with lobate contacts.

Olivine gabbros are the dominant facies in these intrusive bodies. They generally show a magmatic foliation defined by tabular plagioclase laths and elongate olivine aggregates (Fig. 20A and B). Coarse olivine grains are commonly surrounded by cumulus plagioclase laths and clinopyroxene grains (Fig. 20A). Orthopyroxene may be an accessory mineral.

In the southwestern part of the studied area, the gabbroic plutonic sequence is practically unaltered, whereas in the southeastern part (near the village of Hesar), secondary minerals such as calcite, chlorite, clay minerals are abundant, and accompanied by numerous hydrothermal veins of tremolite-actinolite and prehnite.

Olivine comprises about 35–45% of these rocks, and represents the main cumulus phase. The coarser olivine grains may show kink-band deformations (Fig. 20C), a process described by Hunter (1996) as a deformation acquired during compaction of the crystal mush, the olivine grains developing subgrain walls normal to the main compaction stress. The mosaic textures reflect active grain-boundary migration, indicating that solidus to hypersolidus conditions prevailed for a comparatively long time in the lower magma chamber (Boudier et al., 1996). The coarser olivine grains have a nearly constant chemical composition: (Fo76) at the base, and (Fo78) at the top of the layered gabbro sequence. The fine olivine grains have a slightly more evolved composition (Fo73), and olivine inclusions in plagioclase or sometimes in clinopyroxene crystals (Fig. 20B) have a (Fo77) composition. Clinopyroxene crystals have a diopsidic composition (Wo48Fr7En45). Orthopyroxene, as an intercumulus phase, has an bronzitic composition: (Wo2Fr23En75) at the base and (Wo3Fr28En69) at the top of ferrogabbros, reflecting slight magmatic differentiation.

The tabular plagioclase laths, showing no zoning at all, have an anorthitic to bytownitic composition (An91 to

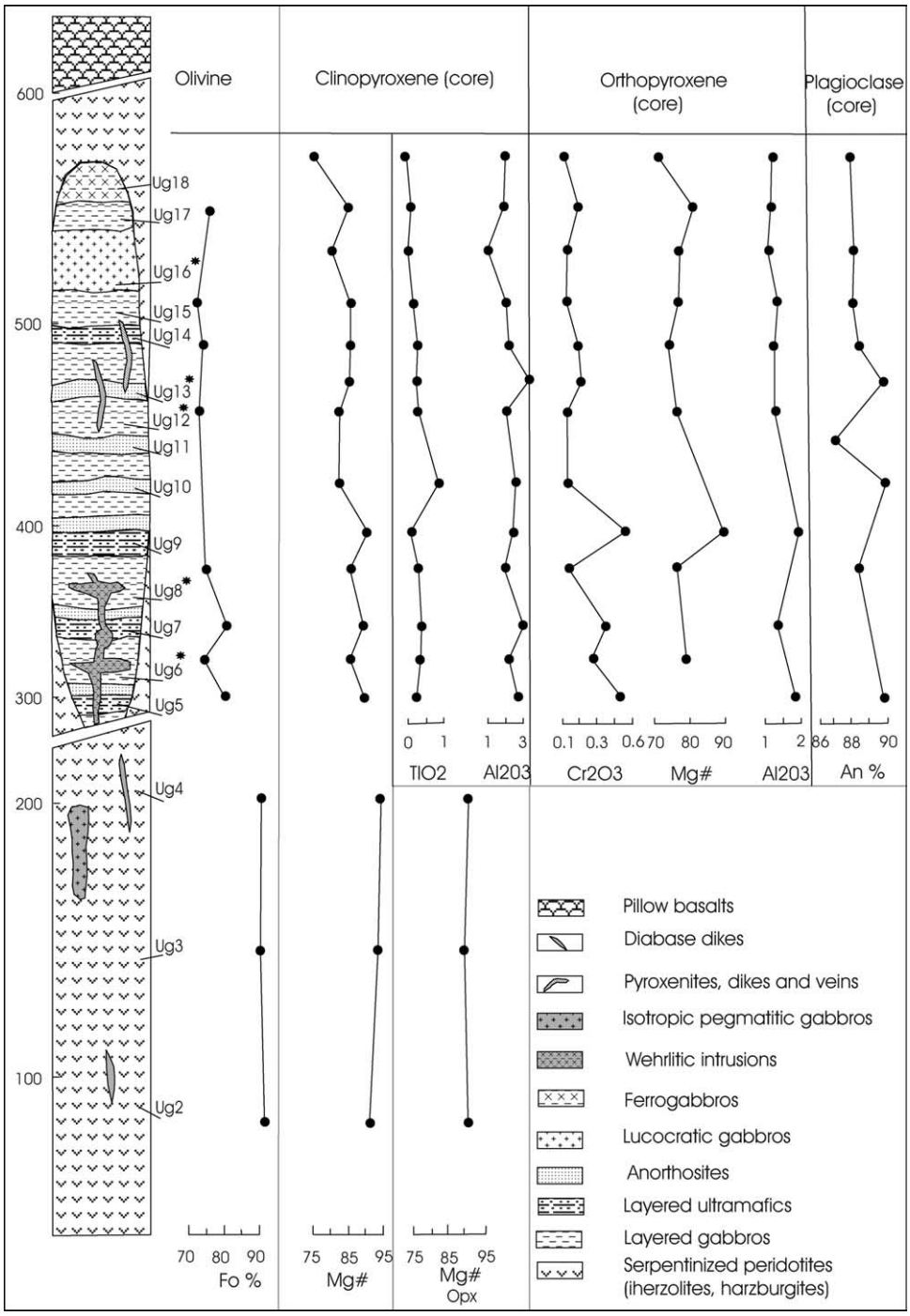

Fig. 4. Cryptic variations of the main silicate phases in the mantle peridotites and cumulate gabbros of the Late Cretaceous ophiolite of Khoy. The location of several analyzed samples (Table 1) are reported on the synthetic log (left column).

An87), and inclusions of plagioclase in clinopyroxene or orthopyroxene have anorthitic compositions (An93). In the lower part of the olivine gabbros, the plagioclase laths show traces of plastic deformation marked by serrated plagioclase-plagioclase grain boundaries, undulose extinctions, and development of tapered twins, a textural type also seen in the layered gabbros from sills in the Moho transition zone of the Oman ophiolite (Boudier et al., 1996). Abundant inclusions of small olivine crystals in the plagioclase and clinopyroxene phases indicate that olivine was the first cumulus phase, followed by plagioclase (inclusions in the clinopyroxenes). Clinopyroxene occurs as both cumulus and intercumulus phases, and orthopyroxene forms the last intercumulus phase with Ti-magnetite grains.

Layered wehrlites are interbedded with olivine gabbros and anorthosites. They have cumulate mosaic textures

and exhibit magmatic layering. Olivine and clinophyroxene are the main mineral phases, with orthopyroxene and some Cr-spinel as accessory minerals. Strongly serpentinized olivine crystals and accessory Cr-spinel grains form the cumulus phases, and clinopyroxene appears as the intercumulus phase. The olivine composition ranges from (Fo81) at the base to (Fo74) at the top of one of the layered wherlites. The average chemical composition of clinopyroxene remains constant (Wo47Fr4En49). There are no crystal zonings or resorptions in the mineral phases. The composition of the accessory orthopyroxene varies from (Wo2Fr16En82) at the base to (Wo2Fr10En88) in the middle of the plutonic sequence, in accordance with the olivine cryptic variations.

Leucocratic coarse-grained gabbros appear commonly in the upper part of the gabbroic sequence. They have mesocumulus textures (Fig. 20D and G), and consist of plagioclase and clinopyroxene, without any olivine. The tabular plagioclase laths have anorthitic to bytownitic compositions (An91 to An78). The clinopyroxene grains have diopsidic compositions ranging between (Wo50Fr10En40) and (Wo46Fr8En46).

Thin, whitish layers of *anorthosites* are abundant in the middle of the layered gabbro sequence, and disappear progressively at the top of the series. These rocks are composed of plagioclase (almost 90% in volume) with minor clinopyroxene. Under the microscope, the plagioclase laths are devoid of zoning, showing polygonal planar boundaries meeting at triple junctions (Figs. 5 and 20). This texture is not due to recrystallization in the metamorphic domain (Passchier and Trouw, 1995), but rather the result of progressive changes of crystal shapes and packing during compaction (Hunter, 1996). About ten percent of clinopyroxene grains fill the spaces as an intercumulus phase. The plagioclase crystals are commonly altered to prehnite, calcite, sericite and sometimes albite, through an abundant network of fine cracks. This hydrothermal alteration is reflected in the compositional variations of the plagioclase phase, ranging from bytownitic compositions (An 86–88) for unaltered plagioclase, to oligoclase (An25) in altered laths. As usual, the clinopyroxene is resistant to alteration and shows rather homogeneous compositions, ranging from (Wo38Fr19En43) to (Wo45Fr9En46).

Ferrogabbros are exposed at the top of the plutonic sequence in the layered gabbros. They are composed of fine-grained plagioclase laths, clinopyroxene and abundant Ti-magnetite grains (Fig. 20F). Plagioclase laths and inclusions of plagioclase in clinopyroxene have homogeneous bytownitic compositions (An87–88). The clinopyroxene grains and inclusions in the plagioclase laths have homogeneous compositions: (Wo41Fr14En45). The Ti-magnetite contains about 7% TiO_2 in average. The order of crystallization was: plagioclase–clinopyroxene–Ti–magnetite.

Pyroxenites exposed as small veins and dikes have coarse-grained, granular to mosaic textures. They are composed of clinopyroxene (Wo44Fr12En44) as the cumulus phase, and of orthopyroxene as the intercumulus

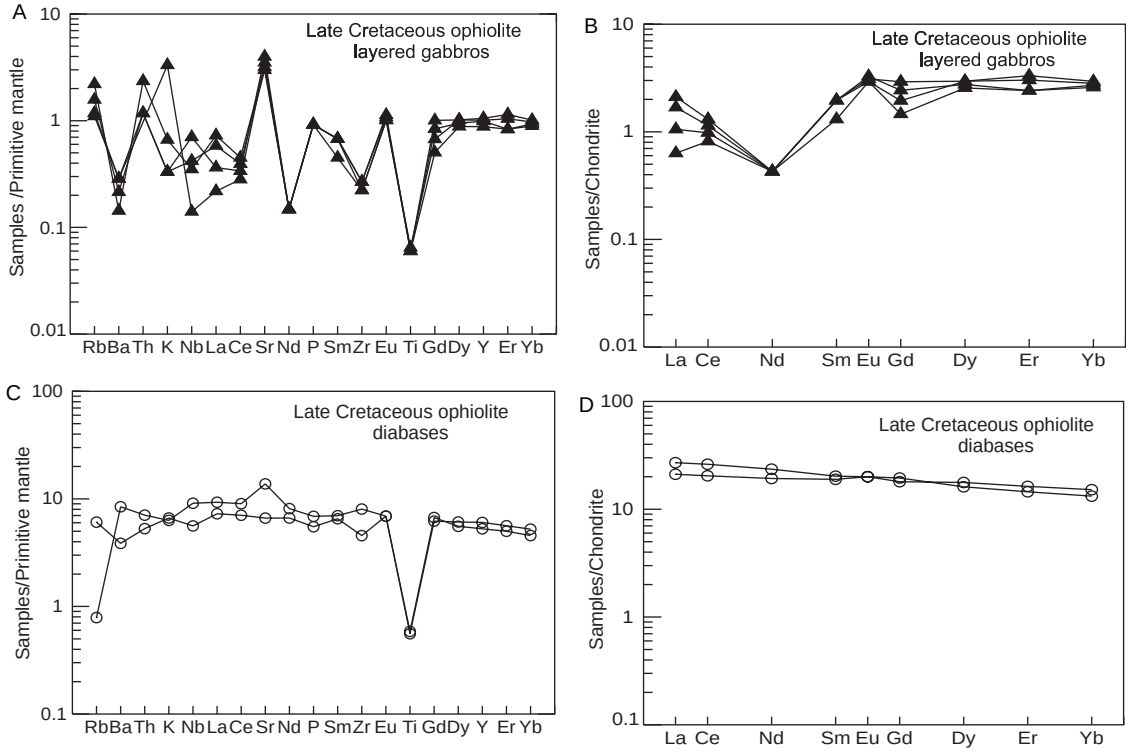

Fig. 5. Multi-element plots and REE profiles of four gabbros from the Late Cretaceous ophiolite of Khoy (top), and of two diabase dikes crosscutting the layered gabbros (bottom).

phase (Wo3Fr27En70). Fine Cr-spinel grains and sphene are the accessory minerals. Orthopyroxene is more or less altered to bastite. We could not find any olivine in the matrix.

Pegmatitic gabbros crosscutting the plutonic sequence are mainly composed of plagioclase, clinopyroxene and orthopyroxene. Rounded olivine inclusions are abundant in clinopyroxene crystals (Fig. 20G). The pegmatitic plagioclase laths have a bytownitic composition (An87–88), and the clinopyroxenes have a diopsidic composition ranging from (Wo42Fr10En48) to (48Fr7En45). The medium-grained orthopyroxene crystals have an enstatitic composition (Wo2Fr19En79). Small dunitic inclusions in the pegmatitic gabbros, showing crenulated margins, have a (Fo77) olivine composition, suggesting that evolved dunitic layers in the magma chamber were removed by these late gabbroic liquids.

Isolated diabase dikes crosscut the layered gabbros. They are generally tectonized (boudinage) and altered. Under the microscope (Fig. 20H), relics of a doleritic texture with primary plagioclase and clinopyroxene are still recognizable (with Ti-magnetite) among the secondary hydrothermal phases (chlorite, calcite, sericite, epidote, quartz, sphene and apatite).

2.3. Crystallization sequence and cryptic variations in the layered gabbroic bodies

Fig. 4 shows the schematic magmatic stratification observed in the layered gabbro bodies intruding the residual mantle peridotites: typically less than one km thick, they consist of alternating layered wehrlites, olivine gabbros and anorthosites, forming decametric to hectometric rhythmic cycles, grading upward to alternating olivine gabbros and anorthosites, to leucogabbros and finally to ferrogabbros at the top.

In the layered wehrlites, the cumulus phases are olivine and accessory Cr-spinel, and the intercumulus phase is clinopyroxene. Plagioclase is generally absent and may appear as inclusions in clinopyroxene.

In the layered olivine gabbros, olivine, plagioclase and clinopyroxene form the cumulus phases, with generally adcumulate to mesocumulate textures. The recurrence of layered wehrlites several times in the gabbroic sequence suggests repetitive inputs of primitive melt into the magma chamber. These olivines have high-Mg compositions and co-crystallized with accessory Cr-spinel as early phases from primitive melts. Cr-spinel ceased to crystallize when clinopyroxene appeared on the liquidus (Pallister et al., 1981; Parlak et al., 1996).

Plagioclase was the second silicate phase to crystallize in the gabbroic sequence. Plagioclase crystals have tabular shapes, with high-Ca compositions (generally with An% > 86), and are sometimes adcumulus phases. In the plutonic sequence, there are recurrent rhythmic layers of wehrlitic, olivine gabbroic, and anorthositic cumulates. The existence of olivine inclusions in the clinopyroxene and plagioclase crystals, and of plagioclase inclusions in clinopyroxene crystals suggests an olivine–plagioclase–clinopyroxene order of crystallization, typical of a MORB-type crystallization trend (Niu and Batiza, 1994).

The Khoy plutonic sequence does not reflect an olivine–clinopyroxene–plagioclase crystallization trend, as reported in immature island-arcs (Elthon, 1991; Pearce et al., 1984; Coleman, 1986; DeBari and Coleman, 1989; Parlak et al., 1996). Orthopyroxenes are observed as cumulus and intercumulus phases, in the layered gabbros and layered wehrlites.

Fig. 4 shows the cryptic variations of the main mineral phases in the layered intrusive bodies, based on electron microprobe analyses realized in the cores of these minerals. We have reported the forsterite content of olivine (Fo), the Mg#, TiO_2 and Al_2O_3 contents of clinopyroxene, the Mg#, Cr_2O_3 and Al_2O_3 contents of orthopyroxene, and the An content of plagioclase (An).

The Fo content of olivine and the Mg# of both clinopyroxene and orthopyroxene are clearly lower than in the mantle unit, and decrease slightly going upsection. These parameters and the Cr_2O_3 content of orthopyroxene have more primitive values in wherlitic layers in the lower part of the section. The Mg# of both pyroxenes and the Cr_2O_3 content of orthopyroxene decrease in the ferrogabbros at the top of the section. The An% of plagioclase cores decreases also from base to top in the gabbroic section, with some irregularities in anorthositic layers probably due to secondary alteration. The Al_2O_3 content in both pyroxenes remains low and does not evolve significantly, suggesting low pressure crystal fractionation (Hess, 1989). The absence of zoning in the cumulus and intercumulus phases suggests a crystallization process under bulk equilibrium conditions at high temperatures, as confirmed by the high Mg/Fe ratios in olivine, and by the high Ca content in plagioclase (Hess, 1989; Parlak et al., 1996).

2.4. Whole rock geochemistry of the gabbroic intrusive bodies

Table 1 gives the whole rock analyses obtained on the layered gabbros and associated intrusive wehrlites.

Fig. 5 presents the multi-element plots and REE profiles of four layered gabbro samples, and two diabase dikes crosscutting the layered gabbros sequence. The gabbros are depleted in incompatible elements, showing very low LILE and REE contents, suggesting that these rocks do not have magmatic liquid compositions, but represent crystal cumulates segregated in the magma chamber. Their REE profiles are flat from Yb to Eu, with an average ratio of two times that of chondrites, and then decrease from Sm to La, with a negative anomaly for Nd. These compositions are compatible with fractionation from N-MORB to T-MORB-type basaltic melts.

Table 1
Representative whole-rock analyses of samples from the plutonic sequence (Late Cretaceous ophiolite of Khoy)

Sample	Ug6	Ug8	Ug12	Ug13	Ug16	Ug19	Ug20	Ug21	Ug22	Ug23	Ug26	Ug27	Ug28	Ug29	Ug30
Rock-type	lg	lg	lg	lg	lg	lg	lg	lg	lg	lg	dia	dia	um	um	um
SiO_2	47.5	47.5	46	45.2	47.5	46.8	47.8	42.5	48.6	48	47.7	47.3	37.5	41.75	42.5
TiO_2	0.13	0.13	0.13	0.05	0.11	0.14	0.13	0.04	0.13	0.16	1.21	1.27	0.012	0.016	0.012
Al_2O_3	14.5	14.55	16.9	29.5	23.25	14.25	16.5	0.74	18.8	17.8	15.75	17.72	0.82	1.29	1.27
Fe_2O_3	6.95	7	7.88	1.81	3.17	6.8	5.7	9.5	5.9	4.9	10.4	9.55	8.2	8.2	7.35
MnO	0.13	0.13	0.13	0.03	0.06	0.12	0.1	0.14	0.12	0.11	0.17	0.15	0.11	0.13	0.12
MGO	13.4	12.85	12.1	2.5	5.7	14.2	11.85	41	9.4	8.7	8	5.92	42	38.75	39.3
CaO	16.4	16.7	15.3	17	17.75	15.85	17.15	3.15	16	18.2	10.8	13.65	1	1.68	2.6
Na_2O	0.55	0.5	0.72	1.54	1.29	0.58	0.6	0.06	0.83	0.89	2.9	2.48	0.015	0.045	0.025
K_2O	0.01	0.02	0.01	0.09	0.02	0.02	0.1	0.01	0.03	0.01	0.2	0.19	0.007	0.02	0.005
P_2O_5	0.02	0.02	0.02	0.01	0.02	0.02	0.02	0.01	0.02	0.02	0.12	0.15	0.014	0.015	0.012
LOI	0.58	0.68	1.06	2.33	1.06	1.33	0.65	2.49	0.31	1.29	2.48	1.87	9.65	7.94	6.57
Total	100.17	100.08	100.25	100.06	99.93	100.11	100.6	99.5	100.14	100.08	99.73	100.25	99.33	99.84	99.76
Rb	0.7	0	1	0.8	0.1	1.4	0.75	2.3	66	0	3.86	0.5	0	0.7	0
Ba	2	2	1.5	9	4	1	2	0	2	5	27	59	0.5	1	0.5
Th	0.1	0	0.1	0	0	0.2	0		0	0	0.45	0.6			
K	83	166	83	747	166	166	830	83	249	83	1660	1577	58.1	166	41.5
Nb	0.3	0.1	0.5	0.1	0	0.25	0.1	0.2	0.2	0.15	4	6.5	0.2	0.2	0.2
La	0.4	0.2	0.25	0.2	0.2	0.5	0.15	0.5	0.3	0.2	5	6.4			
Ce	0.7		0.6			0.8	0.5	1	0.7		12.5	16			
Sr	63	68	84	205	155	67	74	3	98	106	140	291	0.7	4	4.1
Nd	0.2		0.2			0.2	0.2	0.4	0.2		9	11			
Sm	0.3		0.2			0.3	0.3	0.4	0.1		2.9	3.1			
Zr	3	4	2.5	3	4	2.5	3	2	2	4.5	51	90	1.5	2	1.5
Eu	0.18	0.15	0.17	0.1	0.15	0.17	0.19	0.08	0.2	0.15	1.16	1.16			
Gd	0.6		0.3			0.4	0.5		0.6		3.7	4			
Ti	78	78	78	30	66	84	78	24	78	96	726	762	7.2	9.6	7.2
Dy	0.75	0.75	0.65	0.17	0.65	0.75	0.7	0.2	0.7	0.9	4.5	4.1			
Y	4.8	4.2	4	1.2	3.7	4.6	4.5	1	4.3	5.1	27.5	24	0.3	1.7	
Er	0.55		0.4			0.5	0.4	0.1	0.4		2.7	2.4			
Yb	0.5	0.41	0.44	0.12	0.33	0.48	0.46	0.1	0.47	0.52	2.58	2.25			
Sc	45	52	41	9	31	47	44	16	41	48	39	32.5	8.7	13	16
V	150	153	133	35	96	141	135	46	136	159	255	213	42	67	78
Cr	1160	290	228	100	470	870	555	2300	148	99	305	223	2250	2900	2900
Co	50	47	54	7	16	52	40	112	32	26	43	37	112	100	91
Ni	275	162	155	37	60	260	168	2010	70	64	145	42	2300	2050	1950

Symbols: lg, layered gabbro; dia, diabasic dikes; um, ultramafic (wherlitic intrusion).

The diabases also show flat patterns, with a slight positive and regular slope from Yb to La (La/Sm = 1.72–2.06; La/Yb = 1.85–2.66), and a strong negative anomaly for Ti. These rocks have liquid compositions, with REE contents of 15–30 times the chondrites, and T-MORB type profiles, very similar to those of the ophiolitic basalts of the extrusive sequence (see below).

2.5. The extrusive sequence: petrographic facies

The extrusive sequence is entirely basaltic and mainly composed of pillow lava flows (more than 80%), massive flows, sills, sheet flows, fossil lava lakes (10–15%), and hyaloclastic breccias (about 5%). Rare sills of phyric diabases and picrites were observed in some places. We estimate the total thickness of this huge volcanic pile to be between 900 and 1100 m. Lenses of pinkish pelagic limestones interbedded with the lava flows contain microfaunas of Turonian, Santonian, and Campanian age (Khalatbari-Jafari et al., 2004).

On the geological map (Fig. 2), these lavas constitute two volcanic massifs, separated by a saddle covered by Tertiary formations. We name them the *northern volcanic massif* and the *southern volcanic massif*, respectively. Pillow lava tubes dip southward in the northern massif, and dip northward or north-eastward in the southern massif. For us, there is no doubt that both massifs constitute a single and unique ophiolitic extrusive sequence.

Fig. 6 shows the synthetic columns for the four geological sections we have studied in the extrusive sequence, with the location of all analyzed samples. In the southern volcanic massif, we examined one complete section of the entire volcanic pile (Jehennem Dere section, about 900 m thick), and two partial sections (Barajok and Qezel Aqol sections). In the northern volcanic massif, we studied one section (Goldagh section, about 700 m thick), and also collected samples along the Goldagh road.

Along the detailed sections we have done, the basaltic lava pile is characterized by a regular alternation of *phyric basalts* and *aphyric basalts*. Generally speaking, these basalts show a very poor vesicularity, indicating deep oceanic conditions of extrusion. Interbedded sediments between the lava flows are scarce, very thin and always totally pelagic, suggesting again a deep oceanic environment and a rather permanent volcanic activity, preventing sediment deposition on the back of the flows.

We distinguished the following petrographic facies: (1) Megacrysts-bearing phyric basalts and phyric basalts (pillow lavas); (2) aphyric basalts (pillow lavas); (3) microcrystalline basalts (massive flows and sills); (4) phyric diabases (diabase sills); (5) picrites (sills); (6) hyaloclastic breccias; (7) late intrusive diabase dikes.

(1) *Megacrysts-bearing phyric basalts and phyric basalts* are common in both volcanic massifs. In the southern massif (Jehennem Dere, Barajok), plagioclase megacrysts are common in plagioclase-phyric basaltic pillow lavas (Figs. 1 and 21). In the northern massif (Goldagh), clinopyroxene megacrysts are common, surrounded by fine microphenocrysts and microlites of clinopyroxene and plagioclase (Figs. 2 and 21).

Plagioclase megacrysts and phenocrysts have tabular shapes with albite and albite-carlsbad twinning, and normal or reverse zoning (Fig. 21C). Sometimes they exhibit resorption figures and numerous small melt inclusions often arranged in concentric shells (Fig. 21E). These figures were named ‘sieve textures’ by several authors (for example, Shelley, 1993; Nelson and Montana, 1992).

The resorbed plagioclase megacrysts and phenocrysts are highly calcic in composition, from bytownite to anorthite (An84–98), and labradorite to bytownite (An62–76). The non-resorbed, normally zoned plagioclases have a bytownitic composition in the cores (An61–81), and labradoritic compositions in the margins (An55–72). There are also reversely zoned plagioclases, with labradorite to bytownite in the core (An62–76), and bytownite in the margin (An81–84).

The abundance of resorption figures in many pillow samples, with frequent inverse zonings, indicate that disequilibrium processes occurred in the magma chamber due to periodic refilling by new upwelling and more primitive magma, mixing with the evolved magma stored in the magma chamber.

Clinopyroxene megacrysts, up to 5 cm long in the Goldagh section, may also show resorption figures and vary in composition from (Wo36Fr14En50) to (Wo42Fr12En46) in the cores, and (Wo37Fr10En53) to (Wo39Fr18En43) in the margins. Clinopyroxene megacrysts are more abundant in the northern volcanic massif. They are diopsidic in composition, and range from (Wo36Fr10En54) to (Wo46Fr15En39). In the southern massif, they vary from (Wo40Fr12En48) to (Wo48Fr18En34). There are not important differences between core and margin compositions.

Plagioclase microphenocrysts show a wide range of compositions. In the Jehnnem Dere and Barajok sections, we found highly calcic plagioclases with anorthitic composition (An96), and also less calcic compositions (An80–83). In the Qezel Aqol section, we found bytownitic microphenocrysts (An73), and labradoritic ones (An62–67). In the Goldagh section, there are bytownitic (An77) and labradoritic compositions (An51–62).

Clinopyroxene microphenocrysts are abundant in the southern massif, ranging between (Wo39Fr11En50) in Jehnnem Dere and (Wo58Fr15En27) in Qezel Aqol. Plagioclase microlites range from albite (An < 10), to oligoclase (An14–29), andesine (An31–43), and labradorite (An51–68). In Jehennem Dere we found bytownitic compositions (An84). The fine clinopyroxene grains in the groundmass show also a wide compositional range, from (Wo30Fr25En45) in Goldagh to (Wo47Fr15En38) in Jehennem Dere.

In phyric basalts, we found euhedral to subhedral olivine pesoudomorphs, completely replaced by Fe-oxides, calcite, serpentine and chlorite (Fig. 21G).

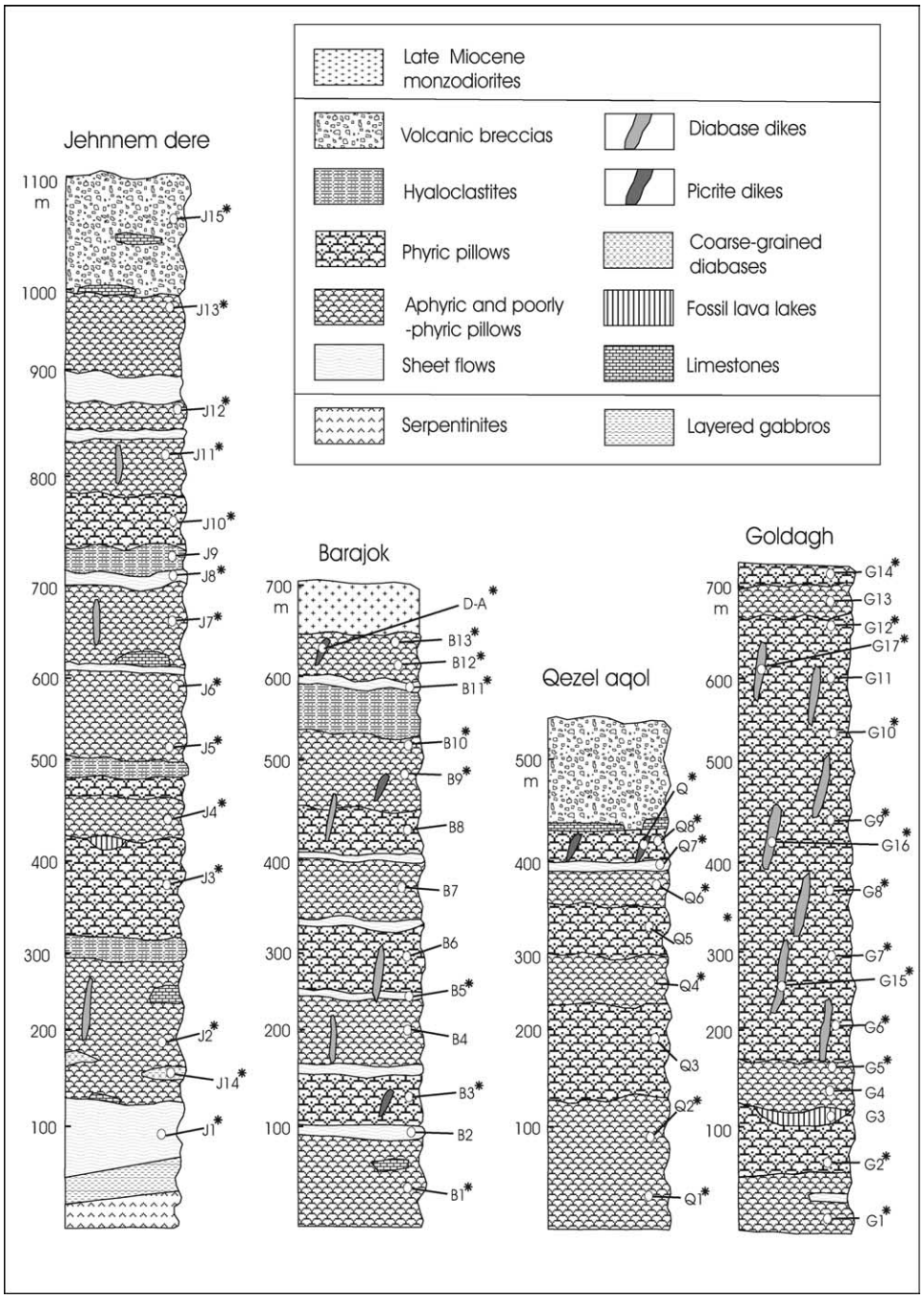

Fig. 6. Synthetic logs of the four geological sections made in the ophiolitic extrusive sequence, and location of the analyzed samples (Table 2A–C).

(2) *Aphyric basaltic* pillow lava flows alternate regularly with the phyric basaltic pillow lava flows all along the sections we have studied, in both volcanic massifs. They have microcrystalline to fluidal textures, and are composed of clinopyroxene and plagioclase as main mineral phases (Fig. 21D). They are more abundant in the southern volcanic massif. Olivine pseudomorphs, made of Fe-oxides, chlorite, calcite and serpentine were observed in these lavas. There are also thin hydrothermal veins made of calcite, chlorite, serpentine, and sometimes zeolites. Sphene, Ti–magnetite and sometimes hematite are the common accessory minerals. The fine grained clinopyroxenes have diopsidic compositions varying from (Wo38Fr21En41) to (Wo47Fr17En36) and sometime ferrosilite composition (Wo8Fr86En6). The microlite plagioclases have wide range compositions from bytownite (An73–84), labradorite (An62–68), to andesine (An45–46), oligoclase (An17–20) and albite (An < 10). In the Goldagh section they have albite (An < 10) to andesine-labradorite compositions. In pillow margins, plagioclase microlites show typical quenched

textures, with 'belt buckles', hollow cores and bifid tips (Fig. 21F), and may exhibit relics of isotropic glass and varioles (Fig. 22B).

(3) *Massive sheet flow basalts* exhibit fine-grained intergranular textures. As in the pillow basalts, plagioclase and clinopyroxene are the main mineral phases, and Fe-oxides with fine-grained sphene are the accessory minerals. They are generally altered to chlorite, calcite, fine-grained clay minerals, sericite, and secondary albite. The clinopyroxene compositions vary from (Wo41Fr22En37) to (Wo44Fr14En62) in the diopside field. The scarce plagioclase phenocrysts show reverse zonings, with labradorite (An68) compositions in the cores and bytownite (An90) compositions in the margins. The plagioclase microlites have albitic (An < 10), and andesine compositions (An43–50).

(4) *Phyric diabases* are exposed as small sills intruded between pillow lava flows. They are more abundant in the southern volcanic massif. The plagioclase phenocrysts are distributed in the fine-grained diabasic groundmass made of plagioclase and clinopyroxene microlites. The plagioclase phenocrysts are altered to sericite, chlorite, epidote, and secondary albite. They show some traces of zoning, preserved by secondary minerals. The less altered parts of the plagioclase laths have labradorite compositions (An54). The microlites of plagioclases have oligoclase (An22) to andesine (An54) compositions. The interstitial clinopyroxene grains have diopsidic compositions (Wo45Fr17En38). Fine sphene grains and prismatic apatite crystals are accessory minerals. Secondary quartz was observed in the groundmass, associated with calcite and chlorite.

(5) A few *picritic sills crop out* among the pillow flows in the southern volcanic massif. The samples are fresh, to poorly altered. These rocks show microgranular to coarse-grained ophitic textures. Olivine, plagioclase and clinopyroxene are the main minerals (Fig. 21H). Olvine crystals have coarse to fine euhedral to subhedral shapes, with homogeneous compositions (Fo80–81). The abundant plagioclase-clinopyroxene clusters indicate contemporaneous crystallization of both minerals. The plagioclase phenocrysts are almost euhedral (tabular shapes) with bytownite compositions (An70–77). The microlites cover a wide range of compositions, from labradorite (An67) to andesine (An38–41) and highly sodic albite (An0.9). Coarse to fine clinopyroxene crystals do not show important compositional variations between the coarse (Wo43–46Fr7–19En38–45) and fine (Wo44–46Fr8–16En40–48) crystals. Opaque minerals with magnetite compositions ($Fe_2O_3 = 56$) are the accessory minerals.

(6) Layered or blocky *hyaloclastic breccias* are interbedded with the pillow lava flows. The most spectacular examples are in the Jehennem Dere section (see our previous paper Khalatbari-Jafari et al., 2004). These autoclastic breccias are composed of angular millimeter to centimeter sized basaltic glassy fragments, devitrified to oxides-hydroxides-smectites mixtures and set in a carbonate matrix (Fig. 22A). The rectilinear morphology of the glass shards and the absence of vesicles indicate deep oceanic hyaloclastites (Honnorez and Kirst, 1975), emplaced at more than 1000 m seawater depth.

(7) *Late intrusive diabase dikes* crosscut the entire volcanic pile. Their thick chilled margins suggest that the volcanic host-rocks were cold during the intrusion. They have doleritic textures, without phenocrysts. These rocks are devoid of olivine (even as pseudomorphs), and are mainly composed of plagioclase, clinopyroxene and iron oxides. The plagioclase laths show a wide compositional range, from highly calcic anorthite (An97–98), to labradorite (An59), andesine (An44) and albite (An2–4). These extreme variations are due to deep, penetrative hydrothermal alterations, with neoformation of albite, clay minerals and sericite. Secondary quartz also crystallized between the mineral spaces as a late hydrothermal phase. The clinopyroxene grains have diopsidic compositions (Wo39Fr18En43 to Wo48Fr19En33) and remain relatively unaltered.

2.6. The extrusive sequence: cryptic variations

The extrusive sequence is about 1 km thick. In order to determine how the basaltic lavas evolved with time along the main sections, we have plotted some geochemical parameters along these sections, combining the whole rock analyses obtained by ICP-AES and the microprobe analyses done on the main mineral phases of the same samples.

The cryptic evolutions are shown in Fig. 7A–D, respectively. Clearly the density of our sampling is too low to record in detail the cyclic variations in the lava pile. However, these diagrams give some information about the general evolution of these basaltic melts from bottom to top:

In the Jehennem Dere section (Fig. 7A), the only complete section we have of the extrusive sequence, cryptic variations show that the basalts did not evolve significantly from the base to top, but seem to be organized in cyclic units, each of them being several hundreds of meters thick.

The Qezel Aqol section (Fig. 7B) show a progressive evolution toward more primitive compositions, at least from Q1 to Q3 samples: the Mg# and An% increase regularly, whereas the Y contents decrease. This 'reverse' evolution may indicate magma mixing processes. Higher in the section, oscillations from more evolved compositions to more primitive ones suggest inputs of primitive magma in the magma chamber, followed by magma mixing processes.

The Barajok section (Fig. 7C) shows similar oscillations, with a slow decrease in Mg# (whole rocks, cpx) from base to top.

In the northern massif, the Goldagh section (Fig. 7D) shows a progressive and moderate decrease of the Mg# (whole rocks), with some superimposed cycles (sample G8, for instance, probably marks the fractionated top of a cycle).

In summary and as a first approximation, it appears that, going upsection, the average composition of the basalts

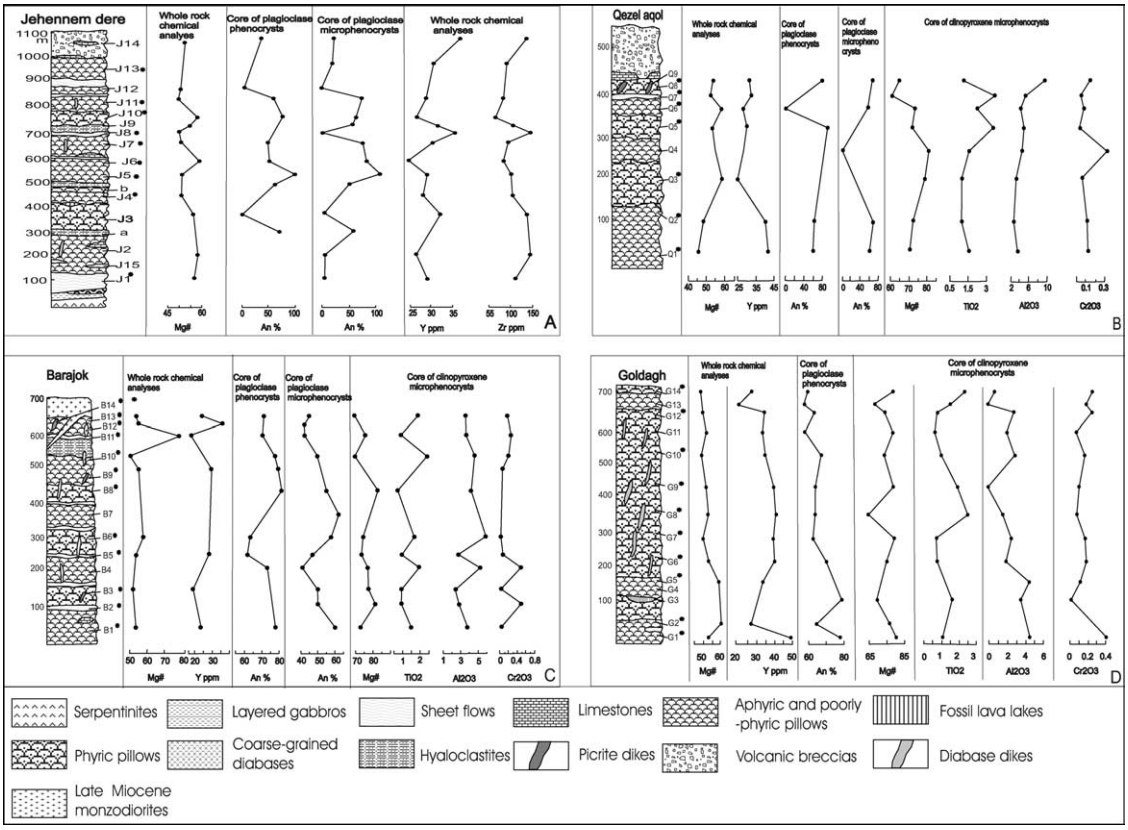

Fig. 7. Cryptic variations along: (A) the basalts of the Jehennem Dere section; (B) the basalts of the Qezel Aqol section; (C) the basalts of the Barajok section; (D) the basalts of the Goldagh section.

remained buffered around moderately fractionated values, without overall evolution of the basaltic pile towards fractionated end-members. More or less pronounced fluctuations around this average composition appear in all the sections, suggesting the existence of magmatic cycles, and of recurrent periods of primitive magma inputs into the magma chamber. The abundance of resorbed and inversely zoned plagioclase and clinopyroxene phenocrysts observed in these lavas is in agreement with this hypothesis.

The regular alternation, along the sections, of phyric flows and aphyric flows suggests important periods of residence of the magma in the magma chambers, favouring the growth of phenocrysts, and allowing time for the plagioclase phenocrysts to float and gather slowly at the roof of the magma chambers. During each submarine eruption, the magma chamber would be tapped twice: (a) first the magma chamber would expel the highly phyric magma accumulated at its roof; (b) next, the chamber expels the poorly phyric to aphyric magma that accumulated in its core.

2.7. Crystal generation in the extrusive sequence

The combined evidence from petrographic observations under the microscope and crystal chemistry (by electron microprobe analyses) suggests the existence of four main crystal generations in the phyric lavas, as shown for the Goldagh section in Fig. 8A and B.

The first generation consists of large, often resorbed, highly calcic plagioclase (anorthite–bytownite), forsteritic olivine and Mg-rich clinopyroxene megacrysts.

The second generation includes plagioclase phenocrysts normally or reversely zoned, most of them crystallized in disequilibrium fractionation systems.

The third generation comprises the clusters of plagioclase and clinopyroxene microphenocrysts, probably crystallized in the subvolcanic conduits during submarine volcanic eruptions.

The fourth generation is composed of microlitic plagioclase and clinopyroxene crystals, which show a wide range of compositions. Field relationships and chemical analyses of samples indicate that the evolved magmas that collected at the top of the magma chambers were erupted first, followed by the less differentiated magmas.

Magma mixing processes modified the liquid compositions, producing phenocrysts and xenocrysts that are not in equilibrium with them. These processes were studied by Stakes et al. (1984) and Le Roux et al. (2002) in mid-Atlantic ridge basalts, and by Humler and Whitechurch (1988) in Central Indian Ridge basalts. Repeated injections of melt in the magma chamber and successive

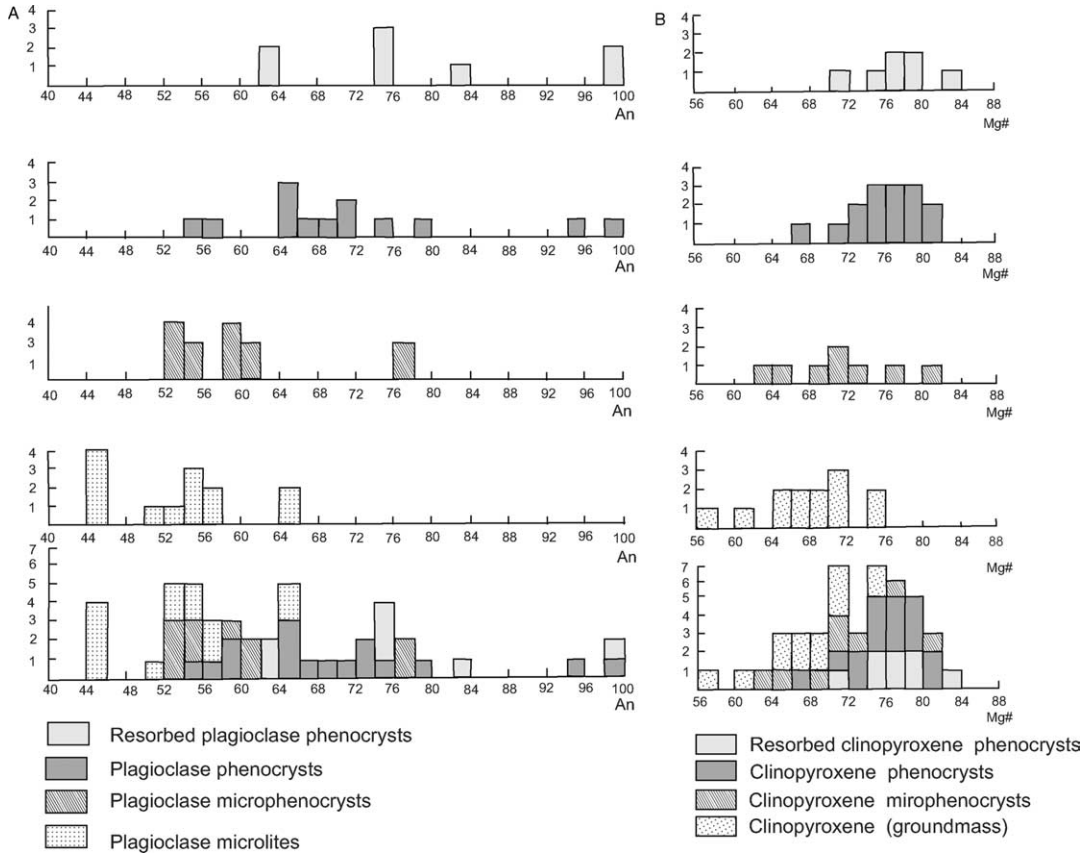

Fig. 8. Frequency diagrams showing the chemical evolution: (A) of the four plagioclase crystal generations (phyric basalts of the Goldagh section); (B) of the four clinopyroxene crystal generations (phyric basalts of the Goldagh section).

replenishments with subsequent mixing events may explain the observed cryptic variations in the extrusive volcanic piles. As described, the first generation of large plagioclase phenocrysts shows resorption figures. These plagioclases contain numerous, small glass inclusions often arranged in concentric shells and embedded by more sodic plagioclases. These figures were described by several authors as 'sieve texture' (Shelley, 1993; Nelson and Montana, 1992) and interpreted as resulting either from magma mixing, or from rapid decompression. The reverse zoning of plagioclases is also considered a result of mixing events (Stewart and Fowler, 2001).

Although the olivine phenocrysts are totally replaced by secondary minerals, petrographic observations indicate that highly calcic plagioclase and olivine phenocrysts were the first mineral phases to form, followed by clinopyroxene. Similar trends were reported from mid-ocean ridge basalts (Niu and Batiza, 1994).

2.8. Geochemistry of the extrusive sequence

All the samples selected for whole rock analyses were taken along four geological sections realized across the extrusive sequence, and also along the road passing through the northern volcanic massif. Fig. 6 shows the precise location of the analyzed samples along the four synthetic logs.

The Jehennem Dere section is the only complete section through the entire volcanic pile, found in the southern volcanic massif. The Barajok and Qezel Aqol sections are partial geological sections in the southern volcanic massif, and the Goldagh section is a partial section, more than 700 m thick, in the northern volcanic massif.

2.8.1. General chemical composition of the lavas

55 new chemical analyses of basaltic lavas, picrites and late intrusive diabase dikes are given in Table 2A–C.

In the (Na_2O+K_2O) vs SiO_2 diagram (Le Bas et al., 1986), the pillow lavas of the Khoy ophiolite cluster in the basaltic domain, with their SiO_2 contents ranging between 45.0 and 50.0 wt% (Fig. 9), except for two samples, whose SiO_2 content may have been modified by circulating fluids: one sample, with a SiO_2 content of 42.6%, plots between picrobasalts and tephrites, and another one, with a SiO_2 content of 52.1%, in the basaltic andesite domain. The two picritic basalts analyzed show lower SiO_2 contents, ranging between 44 and 44.8 wt%.

Most of the basaltic samples are moderately evolved, with Mg# ranging from 62 to 47 (Fig. 10). The two picrites, as expected, have higher Mg# (75 and 79). This moderate

Table 2
Representative whole-rock analyses of samples from the extrusive sequence (Late Cretaceous ophiolite of Khoy)

(A) Sample	J1	J2	J3	J4	J5	J6	J7	J8	J10	J11	J12	J13	J14	J15	B1	B3	B5	B 9	B10
Rock-type	sf	p-a	p-a	p-a	p-a	p-p	p-a	sf	p-p	p-a	p-a	p-a	dia-p	br	p-pp	p-p	sf	p-a	p-a
SiO_2	48.6	46.3	50.9	48.4	46.6	45.3	47.6	48	46.9	45.8	49.8	46.6	46.25	47.5	46.6	47.4	47.4	49	47.5
TiO_2	1.57	1.94	1.83	1.79	1.68	1.5	1.65	1.92	1.18	1.53	1.53	1.66	1.17	1.55	1.02	1.29	1.42	1.58	1.53
Al_2O_3	15.95	15.55	13.68	13.85	15.08	16.15	15.98	13.62	17.6	15.4	15.8	15.14	18.79	14.7	18.48	20.75	16.9	14.95	16.6
Fe_2O_3*	10.95	10.05	11.15	12.18	10.6	11.5	11.54	12.6	9.4	12.14	10.7	11.8	9.82	6.22	9.15	8.05	10.75	10.45	10.2
MnO	0.17	0.16	0.16	0.18	0.18	0.18	0.21	0.18	0.19	0.17	0.12	0.18	0.14	0.13	0.13	0.1	0.19	0.15	0.14
MgO	5.9	5.47	5.3	5.94	5.45	7.7	5.76	6.3	6.1	5.67	4.11	6.44	6.22	3.88	4.75	3.75	6.1	5.92	4.9
CaO	7.7	9.25	8.54	9.05	11.7	9.2	11.8	8.85	12.4	11.66	9.3	9.95	10.44	14.35	13.35	12.6	10.85	11.33	13
Na_2O	4.29	4.18	4.9	3.54	3.36	2.68	2.75	4.01	2.27	2.72	3.89	3.54	2.97	3.45	2.64	3	3.04	3.48	2.6
K_2O	0.72	1.36	0.79	1.19	0.87	0.7	0.1	0.32	0.06	0.14	0.39	0.29	0.48	0.32	0.27	0.56	0.59	0.2	0.08
P_2O_5	0.18	0.29	0.22	0.22	0.2	0.17	0.19	0.25	0.12	0.17	0.22	0.2	0.13	0.16	0.12	0.16	0.16	0.17	0.18
LOI	3.66	5.36	2.34	3.24	4.32	4.8	3.28	3.79	3.77	4.55	3.86	3.77	3.32	7.74	3.21	1.91	2.6	2.41	3.59
Total	99.69	99.91	99.81	99.58	100.04	99.88	100	99.84	99.99	99.95	99.72	99.57	99.73	100	99.72	99.87	100	99.64	100.32
Mg#	55.67	55.92	52.56	53.2	54.51	60.94	53.77	53.82	60.2	52.12	47.24	55.98	59.62	59.25	54.75	52.05	56.94	56.9	52.82
Rb	9.4	27	7.2	16.5	9	8.2	1	5.6	1.1	1.9	8.2	3.1	8.6	4.8	5.4	5.2	7.8	2.4	0.5
Ba	92	128	70	216	103	71	35	18	19	36	53	31	75	40	63	190	82	38	35
K	5976	11288	6557	9877	7221	5810	830	2656	498	1162	3237	2407	3984	2656	2241	4648	4897	1660	664
Th	1.25	1.1	1.1	1	0.75	0.6	0.65	1.5	0.5	0.6	0.8	0.7	0.4	0.8	0.7	1.05	0.55	0.7	0.65
Nb	8.6	13.5	9.6	10.5	8.7	7.4	8	12.2	4.7	6.3	7	8	4.8	6.8	6	8.2	6.6	7	7.9
La	9.2	13.6	9.1	10.5	9	7.4	8.2	12.4	5	6.8	8.2	8.8	5.8	7.1	7	8.8	6.7	6.2	7.3
Ce	21	31	22.5	24	21.5	17.5	19	28	12	16.5	20.5	20	12.5	18	15	19.5	17	16	17.5
Sr	310	245	102	313	278	237	215	214	186	191	240	315	264	230	204	375	340	223	214
Nd	14	20.5	15.6	15.5	14.2	12	14	18.5	8.8	12.5	15	14.5	9	13	9.4	11.4	11.3	11.8	12.6
Sm	3.6	4.7	4.3	4.1	4	3.3	3.9	4.9	2.8	3.8	4.1	4.1	2.7	3.6	2.8	3.2	3.4	3.65	3.8
Zr	116	148	140	136	128	95	120	161	76	105	96	127	69	108	68	91	96	108	115
Eu	1.32	1.64	1.52	1.51	1.47	1.28	1.46	1.71	1.06	1.41	1.46	1.46	1.03	1.35	1.06	1.23	1.3	1.38	1.36
Gd	4.7	4.05	5.4	5	4.95	4.15	5.15	5.7	3.6	4.75	5.1	4.85	3.45	4.55	3.7	3.7	4.3	4.8	4.5
Ti	9420	11640	10980	10740	10080	9000	9900	11520	7080	9180	9180	9960	7020	9300	6120	7740	8520	9480	9180
Dy	5.05	4.65	5.65	5	5.25	4.3	5.45	6.15	3.9	5.1	5.5	5.4	3.5	4.7	4.1	3.65	4.7	5.3	5
Y	29	26	33	29	30.5	25	32	36.5	23.5	30	31	32	20.5	26.5	24	19.8	28	32	29
Er	2.9	2.6	3.3	2.7	3	2.4	3.1	3.4	2.2	2.9	2.9	3.2	1.95	2.7	2.4	2	2.8	3.1	2.8
Yb	2.74	2.15	3.08	2.59	2.87	2.29	3	3.37	2.16	2.75	2.64	3.01	1.79	2.43	2.32	1.76	2.65	3	2.67
Sc	37	29	40	37	39.5	37	40	40	36	39	36	39	32	36	33	23.5	37	45.5	38
V	2.5	188	275	265	264	248	270	291	230	259	280	260	192	210	212	170	245	300	254
Cr	132	175	170	195	198	218	214	186	215	228	215	210	218	204	220	83	210	223	256
Co	37	36	41	40	42	43	41	40	42	48	28	41	38	79	36	29	38	49	41
Ni	42	47	34	46	52	71	69	50	106	70	45	65	52	53	86	38	52	62	83
(La/Sm)m	1.65	1.87	1.37	1.66	1.45	1.45	1.36	1.64	1.15	1.16	1.29	1.39	1.39	1.27	1.62	1.78	1.27	1.1	1.24
(La/Sm)c	1.65	1.87	1.37	1.65	1.45	1.45	1.36	1.63	1.15	1.16	1.29	1.39	1.39	1.27	1.61	1.78	1.27	1.1	1.24
(La/Yb)m	2.41	4.54	2.12	2.91	2.25	2.32	1.96	2.64	1.66	1.77	2.23	2.1	2.33	2.1	2.17	3.59	1.81	1.48	1.96
(La/Yb)c	2.41	4.54	2.12	2.91	2.25	2.32	1.96	2.64	1.66	1.77	2.23	2.1	2.32	2.1	2.16	3.59	1.81	1.48	1.96
Cao/Al_2O_3	0.48	0.59	0.62	0.65	0.78	0.57	0.74	0.65	0.7	0.76	0.59	0.66	0.56	0.98	0.72	0.61	0.64	0.76	0.78
La/Yb	3.36	6.33	2.95	4.05	3.14	3.23	2.73	3.68	2.31	2.47	3.11	2.92	3.24	2.92	3.02	5	2.53	2.07	2.73

La/Sm	2.56	2.89	2.12	2.56	2.25	2.24	2.1	2.53	1.79	1.79	2	2.15	2.15	1.97	2.5	2.75	1.97	1.7	1.92
Zr/Nb	13.49	10.96	14.58	12.95	14.71	12.84	15	13.2	16.17	16.67	13.71	15.88	14.38	15.88	11.33	11.1	14.55	15.43	14.56
Ce/Yb	7.66	14.42	7.31	9.27	7.49	7.64	6.33	8.31	5.56	6	7.77	6.64	6.98	7.41	6.47	11.08	6.42	5.33	6.55
Zr/Nb	13.49	10.96	14.58	12.95	14.71	12.84	15	13.2	16.17	16.67	13.71	15.88	14.38	15.88	11.33	11.1	14.55	15.43	14.56
Ce/Y	0.72	1.19	0.68	0.83	0.7	0.7	0.59	0.77	0.51	0.55	0.66	0.63	0.61	0.68	0.63	0.98	0.61	0.5	0.6

Sample symbols: J, Jehennem dere section; B, Barajok section

Rock-type symbols: sf, basaltic sheet flow; p-a, aphyric pillow basalt; p-pp, poorly phyric pillow basalt; p-p, phyric pillow basalt; dia-p, porphyric diabase; br, breccia.

(B) Sample	B11	B12	B13	D-r	D-r	Q1	Q2	Q3	Q4	Q5	Q6	Q7	Q8	Gr2	Gr3	Gr5	Gr6	Gr4
Rock-type	sf	p-p	p-p	p-a	p-a	p-a	p-a	p-pp	p-pp	p-pp	p-pp	d-c	p-pp	p-a	p-p	p-p	p-p	p-p
SiO_2	44	49.4	47.5	45.75	45.8	45.9	64.8	48.3	48.4	51	47	42.2	46.7	47.9	47.8	47.9	49.5	48.5
TiO_2	0.8	2.25	1.49	1.04	1.24	1.97	1.88	1.37	1.69	1.53	1.48	1.74	1.64	1.63	1.64	1.59	1.85	1.77
Al_2O_3	12.05	15.15	16.55	20	15.8	14.4	14.2	17.3	15.45	15.7	16.2	15.84	16.25	14.3	14.7	15.65	14.6	15.2
Fe_2O_3*	11.55	11.45	10.4	7.75	10.6	13.4	13.05	8.25	11.4	8.05	10.45	11.4	10.05	11.6	11.9	11.5	12	11.4
MnO	0.17	0.17	0.16	0.12	0.18	0.2	0.2	0.11	0.16	0.16	0.14	0.17	0.16	0.2	0.19	0.21	0.19	0.19
MgO	18.6	5.18	5.5	4.84	7.12	5	5.28	4.9	5.83	3.97	6.38	5.45	5.17	6.2	6.6	6.16	5.5	5.28
CaO	7.35	10.85	11	13.14	11	11.35	11.5	11.95	9.33	13.55	11.9	11.9	12.3	11	10.33	10.75	9.65	11.15
Na_2O	1.4	3.02	2.65	3.05	2.25	2.66	2.5	3.28	4.24	2.72	2.44	2.91	2.84	3.74	3.42	2.97	3.73	3.47
K_2O	0.08	0.15	0.18	0.23	0.07	0.09	0.08	0.31	0.05	0.1	0.11	0.14	0.1	0.17	0.24	0.11	0.15	0.19
P_2O_5	0.09	0.21	0.16	0.12	0.13	0.2	0.19	0.15	0.18	0.17	0.17	0.2	0.19	0.17	0.17	0.2	0.23	0.2
LOI	3.52	2.3	4.22	3.94	5.31	2.26	3.33	4.1	3.94	2.97	3.94	2.69	2.83	2.99	2.66	2.71	2.21	2.39
Total	99.61	100.13	99.81	99.98	99.5	99.93	99.81	100.06	99.81	99.92	99.91	99.44	99.53	99.9	99.73	99.75	99.61	99.74
Mg#	78.96	51.32	55.21	59.27	61.02	46.51	48.53	58.06	54.38	53.47	58.73	52.7	54.52	55.47	56.38	55.52	51.65	51.91
Rb	2.3	1.55	1.5	3.4	0.5	1.1	0.7	5.1	1.1	1.4	0.5	1	0.8	1.8	2.2	0.6	2.05	2.35
Ba	30	34	44	32	19	20	17	36	27	38	32	38	35	30	77	30	33	32
K	664	1245	1494	1909	581	747	664	2573	415	830	913	1162	830	1411	1992	913	1245	1577
Th	0.3	0.45	0.65	0.2	0.4	0.35	0.45	0.6	1.05	0.55	0.55	0.65	0.7	0.6	0.45	0.7	0.7	0.7
Nb	3.2	7.7	7	4.4	5	6.1	5.8	5.8	9	6.2	6.4	7.8	7	6	5.6	7.1	8	6.9
La	3	6.2	6.8	4.5	5.4	6.2	6	6.1	10	7.4	6.4	7.9	7.4	6.2	6	7.1	8	6.5
Ce	8	17.5	16	11.5	12.5	17	17	15.8	21.5	18.5	16	20	18.5	16	15.5	19	21	17.5
Sr	119	184	196	319	165	148	131	265	101	210	180	212	212	256	245	186	216	192
Nd	5.8	14.5	11.5	8.3	9.7	14.5	14	12	14	14	12.3	15	14	12.5	12.5	14.8	16.7	14.5
Sm	2	4.4	3.4	2.3	3	4.6	4.4	3.3	3.75	4	3.6	4.2	4	4	4	4.6	5.2	4.4
Zr	55	145	97	65	83	118	119	86	109	110	97	130	119	120	120	130	152	132
Eu	0.75	1.72	1.26	0.95	1.1	1.64	1.61	1.22	1.39	1.44	1.34	1.58	1.47	1.45	1.44	1.5	1.7	1.6
Gd	2.35	6.2	4.3	2.95	3.75	6.2	6.2	4.4	4.7	5.05	4.6	5.5	5.2	5.2	4.95	5.8	6.9	5.8
Ti	4800	13500	8940	6240	7440	11820	11280	8220	10140	9180	8880	10440	9840	9780	9840	9540	11100	10620
Dy	2.6	6.6	4.55	3.05	4.1	7	6.9	4.25	4.95	5.1	4.9	5.9	5.55	5.8	5.8	6.65	7.7	6.85
Y	15	37.5	26	18	24	42.5	41	24.5	29.3	30	29	34.5	32.5	35	35.5	40.5	45.5	41
Er	1.5	3.7	2.5	1.7	2.4	4.15	4	2.6	2.8	3	2.7	3.4	3.1	3.5	3.5	4	4.6	4.2
Yb	1.45	3.46	2.46	1.67	2.3	4.05	3.94	2.3	2.69	2.65	2.67	3.24	3.02	3.4	3.36	3.83	4.4	3.86
Sc	24	46.5	39	27	38.5	43	42.5	34	39	37	38	41	39.5	43	42	36	37	40
V	143	420	272	170	245	370	348	235	274	250	252	281	265	294	290	254	298	302
Cr	600	198	205	197	230	124	131	200	124	225	228	220	224	235	237	182	140	180
Co	85	66	44	39	43	43	41	46	37	73	42	42	43	41	45	43	42	42
Ni	550	66	61	100	86	55	55	75	41	92	98	61	69	59	63	87	66	67
(La/Sm)m	0.97	0.91	1.29	1.26	1.16	0.87	0.88	1.19	1.72	1.2	1.15	1.22	1.2	1	0.97	1	0.99	0.95
(La/Sm)c	0.97	0.91	1.29	1.26	1.16	0.87	0.88	1.19	1.72	1.19	1.15	1.21	1.19	1	0.97	1	0.99	0.95
(La/Yb)m	1.48	1.29	1.98	1.93	1.68	1.1	1.09	1.9	2.67	2	1.72	1.75	1.76	1.31	1.28	1.33	1.3	1.21

(*continued on next page*)

Table 2 (*continued*)

(B) Sample	B11	B12	B13	D-r	D-r	Q1	Q2	Q3	Q4	Q5	Q6	Q7	Q8	Gr2	Gr3	Gr5	Gr6	Gr4
Rock-type	sf	p-p	p-p	p-a	p-a	p-a	p-a	p-pp	p-pp	p-pp	p-pp	d-c	p-pp	p-a	p-p	p-p	p-p	p-p
(La/Yb)c	1.48	1.29	1.98	1.93	1.68	1.1	1.09	1.9	2.67	2	1.72	1.75	1.76	1.31	1.28	1.33	1.3	1.21
Cao/Al_2O_3	0.61	0.72	0.66	0.66	0.7	0.79	0.81	0.69	0.6	0.86	0.73	0.75	0.76	0.77	0.7	0.69	0.66	0.73
La/Yb	2.07	1.79	2.76	2.69	2.35	1.53	1.52	2.65	3.72	2.79	2.4	2.44	2.45	1.82	1.79	1.85	1.82	1.68
La/Sm	1.5	1.41	2	1.96	1.8	1.35	1.36	1.85	2.67	1.85	1.78	1.88	1.85	1.55	1.5	1.54	1.54	1.48
Zr/Nb	17.19	18.83	13.86	14.77	16.6	19.34	20.52	14.83	12.11	17.74	15.16	16.67	17	20	21.43	18.31	19	19.13
Ce/Yb	5.52	5.06	6.5	6.89	5.43	4.2	4.31	6.87	7.99	6.98	5.99	6.17	6.13	4.71	4.61	4.96	4.77	4.53
Zr/Nb	17.19	18.83	13.86	14.77	16.6	19.34	20.52	14.83	12.11	17.74	15.16	16.67	17	20	21.43	18.31	19	19.13
Ce/Y	0.53	0.47	0.62	0.64	0.52	0.4	0.41	0.64	0.73	0.62	0.55	0.58	0.57	0.46	0.44	0.47	0.46	0.43

Sample symbols: B, Barajok section; D-r, Road of Dizaj-e-Aland; Q, Qezel Aqol section; Gr, Road of Goldagh.

Rock-type symbols: sf, basaltic sheet flow; p-a, aphyric pillow basalt; p-pp, poorly phyric pillow basalt; p-p, phyric pillow basalt.

(C) Sample	Gr1	Gr7	G1	G2	G5	G6	G7	G8	G9	G10	G11	G12	G14	G16	G17	G15	Q	D-A
Rock-type	p-a	p-p	p-a	p-p	p-pp	p-p	p-p	p-p	p-p	p-p	p-p	p-p	p-p	dia	dia	dia	pic	Pic
SiO_2	47.8	47.5	47.2	46.7	47.8	49	48.5	48	52.7	48	49	47.5	48.5	52.1	47.65	52.1	44	44.8
TiO_2	2.23	2.15	2.35	1.17	1.61	1.79	1.77	1.79	1.85	1.79	1.56	1.72	1.84	0.92	0.88	1	0.85	0.78
Al_2O_3	14.15	13.3	13.8	18.2	15	15	14.72	15	14.45	15.5	16.25	15.9	14.15	15	15.15	14.65	11.7	15.25
Fe_2O_3*	13.95	12.25	13.5	9.62	11.7	11.4	12.16	10.82	12.95	12.25	10.9	11.84	12.3	12.45	11.9	12.65	11.14	10.8
MnO	0.22	0.2	0.19	0.14	0.18	0.21	0.21	0.22	0.24	0.2	0.2	0.17	0.21	0.2	0.21	0.21	0.16	0.15
MgO	5.24	5.17	6.54	6.2	7.08	5.48	5.42	5.14	5.85	5.33	4.91	5.08	5.02	4.9	3.76	4.06	19	14.5
CaO	10.6	9.45	9.65	11.8	10.9	11.85	11.58	12.4	10.5	10.65	11.7	12	11.05	5.81	5.55	6.27	7.1	9
Na_2O	3.27	3.79	3.52	2.61	2.68	2.68	2.58	2.7	2.7	2.9	2.62	2.74	2.61	3.9	4.94	4.44	1.5	1.62
K_2O	0.28	0.38	0.14	0.11	0.25	0.1	0.08	0.14	0.16	0.13	0.08	0.15	0.11	1.15	1.74	1.23	0.06	0.1
P_2O_5	0.31	0.21	0.25	0.14	0.17	0.2	0.2	0.21	0.21	0.2	0.18	0.18	0.2	0.35	0.38	0.18	0.1	0.1
LOI	1.77	1.85	2.49	3.01	3.05	3.36	3.4	4.34	2.55	1.91	3.43	2.48	3.32	2.79	2.25	2.39	3.63	2.91
Total	99.82	99.85	99.63	99.7	100.12	100.07	99.92	99.78	99.96	99.56	99.83	99.91	99.81	99.57	99.46	99.78	99.23	100.01
Mg#	46.68	49.59	53.03	60.03	58.51	52.84	50.95	52.54	51.29	50.35	51.22	50	48.75	47.84	42.41	42.79	79.9	75.78
Rb	2.85	6	1.05	0.6	2.1	1.2	0.8	1.6	1.4	1.8	1.1	2.2	1.1	12	21.2	18.6	2.2	2.7
Ba	65	35	27	21	36	23	19	26	29	29	23	32	25	442	560	440	12	20
K	2324	3154	1162	913	2075	830	664	1162	1328	1079	664	1245	913	9545	14442	10209	498	830
Th	1.1	0.55	0.7	0.3	0.45	0.6	0.6	0.8	0.6	0.6	0.45	0.55	0.6	4	4.4	4	0.2	0.3
Nb	12.8	7	9	4.2	5.5	6.6	6.5	6.8	6.9	6.5	6.1	5.7	5.7	4.1	4.7	4.5	3.1	3.7
La	11.8	6.8	8.4	4.4	5.6	6.6	6.6	6.9	7	6.7	6.3	6.4	6.4	22	25	20.5	3.4	4
Ce	29.5	19	22.5	12	15.3	18.5	18	18.5	18	17.5	17.5	17	17.5	41.5	45.5	37	8.5	10
Sr	175	212	229	169	150	143	137	144	135	145	154	154	127	214	187	161	122	181
Nd	22	16	18	9	12.2	15	15	15	15	14.5	13.4	14	15	21	22.5	18.5	6.5	6
Sm	6.3	5	5.45	2.8	4	4.6	4.4	4.8	4.7	4.7	4.2	4.45	4.8	4.65	5	4.5	2.15	1.85
Zr	183	145	160	87	115	128	122	132	140	128	113	118	133	62	68	67	58	55
Eu	3.04	1.81	1.9	1.12	1.36	1.62	1.64	1.64	1.65	1.6	1.47	1.54	1.67	1.44	1.54	1.38	0.77	0.71
Gd	8.3	6.8	7	3.85	5	6	6.1	6.35	6.55	6.3	5.7	5.9	6.6	4.8	5.1	4.6	2.6	2.1
Ti	13380	12900	14100	7020	9660	10740	10620	10740	11100	10740	9360	10320	11040	5520	5280	6000	5100	4680
Dy	9	7.8	8.1	4.15	5.65	6.85	6.8	7.25	7.4	7.1	6.2	6.5	7.4	4.4	4.7	4.4	2.85	2.3
Y	54	46.5	48.5	26	34	41	40.5	43	43	42	36	38	45	25.5	27	26	16.7	13.5
Er	5.4	4.6	4.8	2.4	3.4	4.1	4	4.2	4.3	4.2	3.6	3.75	4.4	2.5	2.7	2.5	1.65	1.3
Yb	5.06	4.54	4.62	2.41	3.17	3.96	3.85	4.07	4.2	3.92	3.45	3.5	4.25	2.35	2.6	2.5	1.59	1.26
Sc	38.5	43	44	33.5	43	38	39	37	41	40	36	39	39	31	29	35	25	22
V	308	387	395	205	290	302	300	295	322	305	265	292	318	340	302	392	146	128

Cr	71	90	132	234	240	165	177	160	167	163	208	212	138	6	5	8	436	332
Co	45	47	40	44	44	44	44	44	42	40	41	38	39	28	27	29	75	68
Ni	37	48	50	101	62	69	72	60	70	63	91	54	54	10	9	8	880	310
(La/Sm)m	1.21	0.88	1	1.02	0.9	0.93	0.97	0.93	0.96	0.92	0.97	0.93	0.86	3.06	3.23	2.94	1.02	1.4
(La/Sm)c	1.21	0.88	1	1.01	0.9	0.93	0.97	0.93	0.96	0.92	0.97	0.93	0.86	3.05	3.23	2.94	1.02	1.4
(La/Yb)m	1.67	1.07	1.3	1.31	1.27	1.2	1.23	1.22	1.2	1.23	1.31	1.31	1.08	6.72	6.9	5.88	1.53	2.28
(La/Yb)c	1.67	1.07	1.3	1.31	1.27	1.2	1.23	1.22	1.2	1.23	1.31	1.31	1.08	6.72	6.9	5.88	1.53	2.28
Cao/Al_2O_3	0.75	0.71	0.7	0.65	0.73	0.79	0.79	0.83	0.73	0.69	0.72	0.75	0.78	0.39	0.37	0.43	0.61	0.59
La/Yb	2.33	1.5	1.82	1.83	1.77	1.67	1.71	1.7	1.67	1.71	1.83	1.83	1.51	9.36	9.62	8.2	2.14	3.17
La/Sm	1.87	1.36	1.54	1.57	1.4	1.43	1.5	1.44	1.49	1.43	1.5	1.44	1.33	4.73	5	4.56	1.58	2.16
Zr/Nb	14.3	20.71	17.78	20.71	20.91	19.39	18.77	19.41	20.29	19.69	18.52	20.7	23.33	15.12	14.47	14.89	18.71	14.86
Ce/Yb	5.83	4.19	4.87	4.98	4.83	4.67	4.68	4.55	4.29	4.46	5.07	4.86	4.12	17.66	17.5	14.8	5.35	7.94
Zr/Nb	14.3	20.71	17.78	20.71	20.91	19.39	18.77	19.41	20.29	19.69	18.52	20.7	23.33	15.12	14.47	14.89	18.71	14.86
Ce/Y	0.55	0.41	0.46	0.46	0.45	0.45	0.44	0.43	0.42	0.42	0.49	0.45	0.39	1.63	1.69	1.42	0.51	0.74

Sample symbols: Gr, Road of Goldagh; G, Goldagh section; Q, Qezel Aqol section; D-A, Dizaj-e-Aland.
Rock-type symbols: p-a, aphyric pillow basalt; p-p, phyric pillow basalt; p-pp, poorly phyric pillow basalt; dia, diabasic dike; pic, picrite.

evolution is confirmed by the Ni contents, which are lower than 100 ppm, and by the TiO_2 contents, which are generally higher than 1.5 wt%. Fig. 10 shows that basalts from the northern volcanic massif (Goldagh section) cover a wider range of fractionation than those from the southern volcanic massif (Jehennem Dere, Barajok and Qezel Aqol sections): the latter do not show Mg# lower than 52 (except one single sample from Qezel Aqol section), whereas the Goldagh basalts evolved towards more fractionated liquids (Mg# = 47).

Fig. 10A and B shows that the compatible elements Cr (230–80 ppm) and Ni (100–40 ppm) exhibit the overall expected positive correlation with Mg#. In Fig. 10C and D, the incompatible elements Zr (50–180 ppm) and TiO_2 show the expected overall negative correlation with the Mg#.

By comparison, the three late intrusive diabase samples exhibit quite distinct characteristics. They do not have basaltic compositions, but plot in the trachy-andesitic basalt or trachybasalts fields, with either higher SiO_2 contents (52%), or higher alkali contents (Fig. 9). They have low Mg# (42–48), very low Ni contents (less than 10 ppm), and also low contents in TiO_2 (less than 1.0%) and Zr (Fig. 10).

Finally, the excellent Ti–Zr positive correlation in the Ti–Zr diagram (Fig. 11) shows that the entire extrusive series constitutes a single magmatic trend, mainly controlled by the fractionation of olivine, plagioclase and clinopyroxene.

Multi-element plots (normalized to primitive mantle) *and REE profiles* (normalized to chondrites) of all analyzed samples from the extrusive sequence are shown in Fig. 12 (southern volcanic massif) and Fig. 13 (northern volcanic massif).

2.8.2. Jehennem Dere section

In the Jehennem Dere samples, the multi-element spidergrams (Fig. 12A) show a complete dispersion pattern for Rb, Ba, Th and K, obviously related to secondary alteration processes, affecting both phyric and aphyric lavas. A weak positive anomaly for Eu may be related to plagioclase accumulation. However, both aphyric and phyric basalts exhibit this anomaly, which does not appear in the REE profiles (Fig. 12B). REE profiles are linear and homogeneous with a moderate positive slope from HREE to LREE, very similar to classical oceanic T-MORB trends. As shown in Fig. 12B, they are distinct from N-MORB trends, since LREE are enriched 20–50 times the chondrite abundances, with (La/Sm) = 1.1–1.6, and (La/Yb) = 1.7–4.5. These REE patterns are all parallel to one another, indicating a fractionated series, where phyric basalts seem to be less evolved than aphyric ones. The less evolved sample is a porphyric diabase, and the most evolved one is a massive sheet flow.

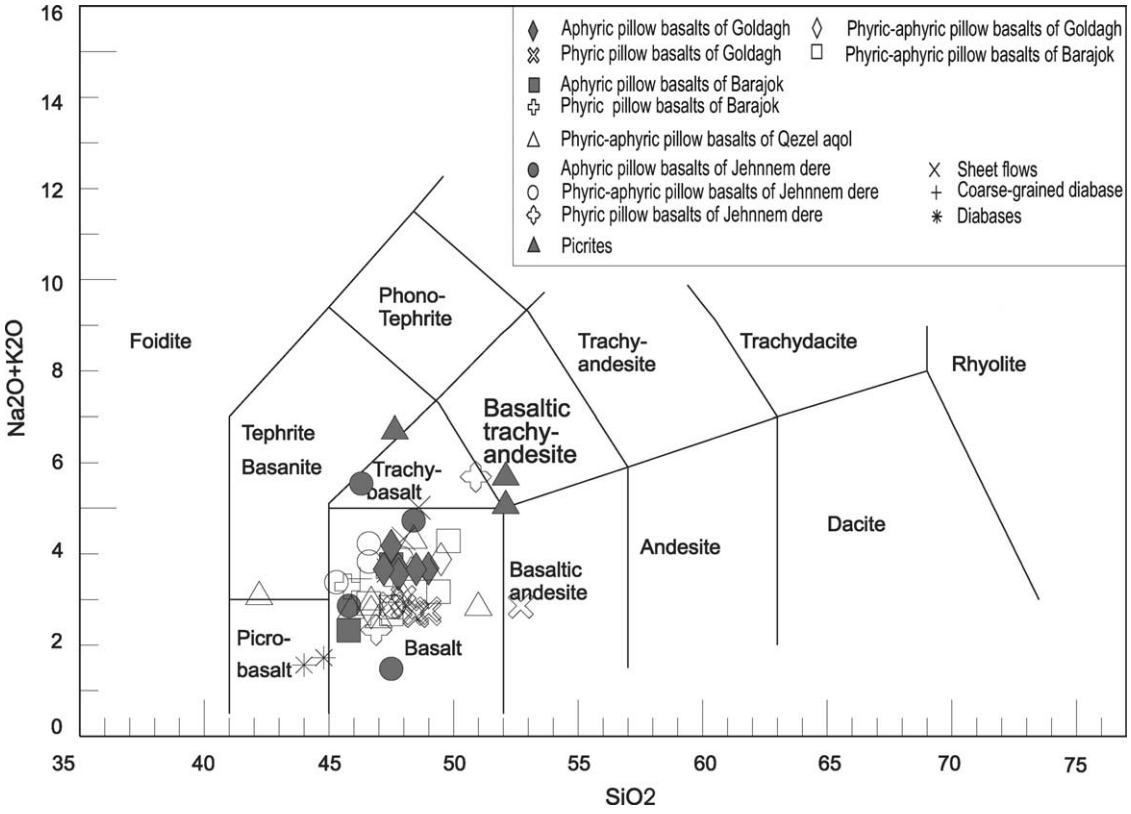

Fig. 9. Plots of the ophiolitic lavas of Khoy (late Cretaceous ophiolite) in the (Na_2O+K_2O) vs SiO_2 diagram (Le Bas et al., 1986).

2.8.3. Barajok section

The basalts and basaltic sheet flows from the Barajok section display uniform compositions (Table 2). They present the same important dispersion for Rb, Ba, Th and K, due to hydrothermal alteration (Fig. 12C). The spidergram patterns from Nb to Yb are slightly flatter than the previous samples, with LREE enriched 15–40 times the chondrite abundances, (La/Sm = 1–1.8), and (La/Yb) = 1.5–3.6 (Fig. 12D). These patterns are somewhat intermediate between N-MORB and T-MORB patterns. Slightly positive Sr anomalies may be due to plagioclase accumulation. The less evolved basalt is a massive sheet flow, and the most evolved one is a phyric basalt. Three samples show a clear depletion in HREE with respect to N-MORBs or T-MORBs.

2.8.4. Qezel Aqol section

The porphyric pillow basalts and basaltic sheet flows from the Qezel Aqol section show uniform patterns with a narrow range of fractionation, similar to the most evolved patterns from the Barajok section.

These lavas are quite unaltered and do not show the irregular dispersion for Rb, Ba, Th, and K (Fig. 12E), seen in Jehennem Dere and Barajok samples. Their patterns show a positive slope from Rb to Th, and a clear negative anomaliy in K, related to the low K character of the original basaltic melt. A small negative Sr anomaly suggests that these samples are plagioclase-poor and poorly phyric. The REE patterns follow more or less the T-MORB trend (Fig. 12F), with LREE enrichment of 20–45 times chondritic abundances, (La/Sm) = 0.9–1.7, and (La/Yb) = 1.1–2.7. Two samples are slightly enriched in HREE with respect to the T-MORB trend.

In the northern volcanic massif, northwest of Kordkandi village, we sampled along the road of Kordkandi to Khan villages, and along the Goldagh section, starting on the road (bottom) and finishing at Goldagh peak (top).

2.8.5. Goldagh section

In Fig. 13A, multi-element plots indicate that the basalts from the northern volcanic massif are much less altered than those from the southern volcanic massif. The multi-element plots are strictly parallel with one another. They are much less dispersed than previous samples for Rb, Ba, Th and K (compare with Fig. 12A and C), in agreement with the unaltered appearance of these lavas under the microscope. They show a positive slope from Rb to Th, a clear negative anomaly for K, and a small negative anomaly for Sr. These profiles are identical to those of Qezel Aqol (Fig. 12E), confirming the genetic link between both the southern and northern volcanic massifs.

The REE patterns (Fig. 13B) are similar to those of the Qezel Aqol section, with (La/Sm) = 0.9–3.2, and (La/Yb) = 1.1–6.9. Remarkably parallel to one another, they are

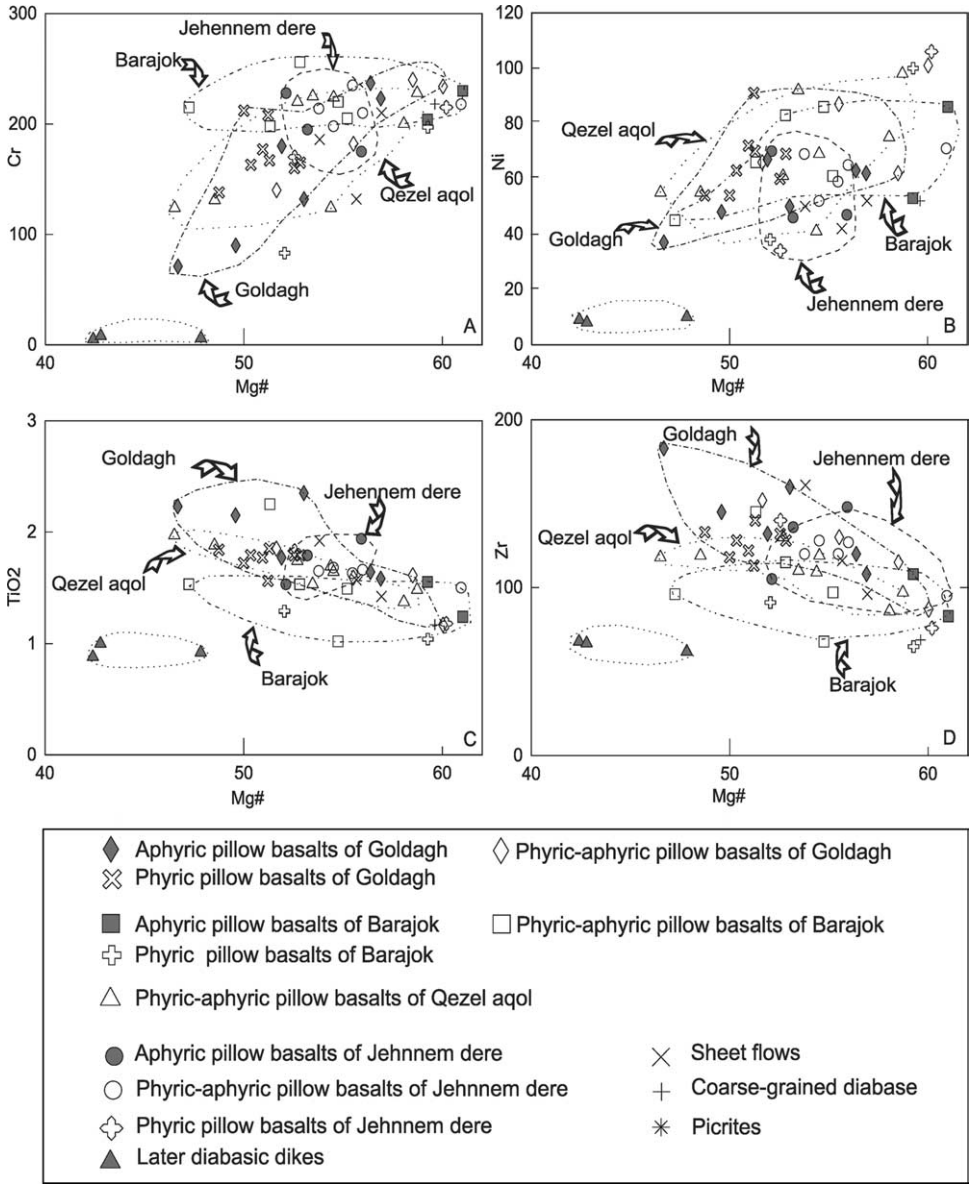

Fig. 10. Plots of the ophiolitic lavas of Khoy (late Cretaceous ophiolite) in the Mg# vs Cr, Ni, TiO_2 and Zr diagrams.

vertically spread, showing a wide range of fractionation. One phyric basalt is depleted in all REE with respect to the group. Another phyric basalt is the most fractionated of all samples. The relative HREE enrichment of Goldagh samples with respect to those of the southern volcanic massif may be due to their higher content in clinopyroxene phenocrysts.

2.8.6. Goldagh road

The pillow basalts exposed along the Goldagh road represent the basal visible part of the northern volcanic massif. The spidergrams show some dispersion for Rb, Ba, Th, and K elements, and rather flat patterns for the other incompatible elements (Fig. 13C). The REE patterns exhibit rather flat patterns similar to those of the Goldagh section (Fig. 13D), with REE abundances ranging from 25 to 50 times chondrite abundances, with enrichment in HREE with respect to T-MORB.

2.8.7. Late intrusive diabase dykes

A number of huge diabasic dikes crosscut the entire volcanic pile. Their thick chilled margins suggest that the volcanic host-rocks were cold during the intrusion. As we have seen, these diabase dikes have trachy-andesitic to trachy-basaltic compositions (Fig. 9), and plot outside the global trends of ophiolitic basalts (Fig. 10). Their spidergrams and REE patterns (Fig. 13E and F) are different from those of the ophiolitic extrusives, with *pronounced slopes typical of calk–alkaline series, strong enrichments in Ba, Th, K and LREE, and clear negative*

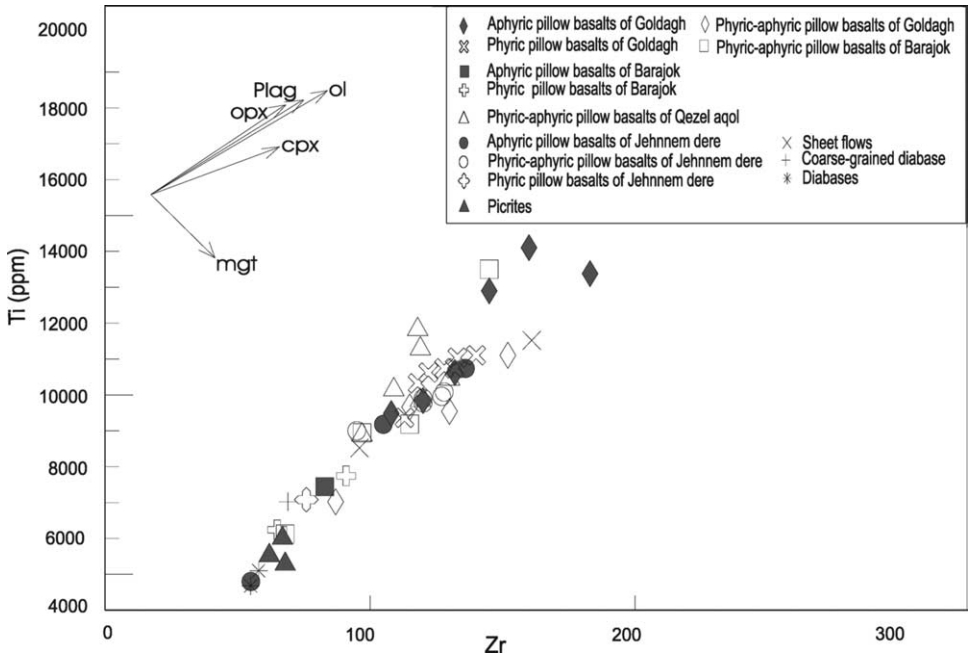

Fig. 11. Plots of the ophiolitic lavas of Khoy (late Cretaceous ophiolite) in the Ti vs Zr diagram.

anomalies for Nb, Zr and Ti, suggesting a 'supra-subduction' environment.

2.9. Tectonomagmatic diagrams

In the Ti/100–Zr–Y.3 diagram (Pearce and Cann, 1973), all the samples, including the late intrusive diabases, plot in the 'ocean floor' field (Domain B in Fig. 14A).

In the Zr/Y versus Zr diagram (Pearce and Norry, 1979), almost all ophiolitic basalt samples cluster inside the MORB domain (Fig. 14B). The late intrusive diabases plot in the overlapped field between MORB and V-AB domains (volcanic-arc basalts).

In the V versus Ti/1000 diagram of Shervais (1982), all the ophiolitic basalt samples plot in the field bracketed between Ti/V = 20 and Ti/V = 50, in the field of 'MORB basalts', whereas the late intrusive diabase samples plot in the field bracketed by Ti/V = 10 and TI/V = 20, in the field of 'arc-volcanism basalts' (Fig. 14C).

3. The supra-ophiolitic series: petrographic study and geochemistry of the lavas

3.1. Sample selection

We distinguished four members in this unit (Fig. 15), which are from bottom to top: (1) the turbiditic series and associated syn-sedimentary breccias containing abundant rounded or angular volcanic fragments (Fig. 22C), (2) epiclastic volcanic breccias and pillow lavas, (3) ankaramitic volcanic breccias, (4) an upper volcanic-sedimentary member. Pelagic limestones associated with this series contain microfaunas of Late Cretaceous to Early Paleocene age (Khalatbari-Jafari et al., 2004). We interpreted this series as a *subduction trench deposit, evolving toward a back-arc environment* (see Khalatbari-Jafari et al., 2004, Fig. 16).

The volcanic samples selected from the 'supra-ophiolitic series' for whole rock analyses were all taken along three geological sections in the southern volcanic massif, above the ophiolitic lavas: the Jehennem Dere, the Qezel aqol and the Abshar-Hesar sections. Fig. 15 shows the precise location of the analyzed samples along the three synthetic logs.

For clarity we plotted the analytical data under four main symbols. The two first symbols represent the volcanic fragments reworked in the turbidites: those showing T-MORB type spidergrams and REE profiles close to those of the underlying ophiolitic lavas (cercles), and those showing a negative Nb anomaly on the spidergrams (triangles). The third symbol represents the pillow lava flows associated with cherts and pelagic limestones (squares), and the fourth symbol represents the ankaramitic breccias and lavas (diamonds).

3.2. Geochemistry of the lavas

The whole rock analyses of this group are given in Table 3.

In the $(Na_2O + K_2O)$ vs SiO_2 diagram (Le Bas et al., 1986), the samples plot in several fields including basalts, trachybasalts, basaltic trachy-andesites and trachy-andesites (Fig. 16). The pillow lavas and 'normal' volcanic fragments reworked in the turbidites plot in the basalt and trachy-basalt fields ($SiO_2 < 50.5\%$); the Nb-poor volcanic fragments from

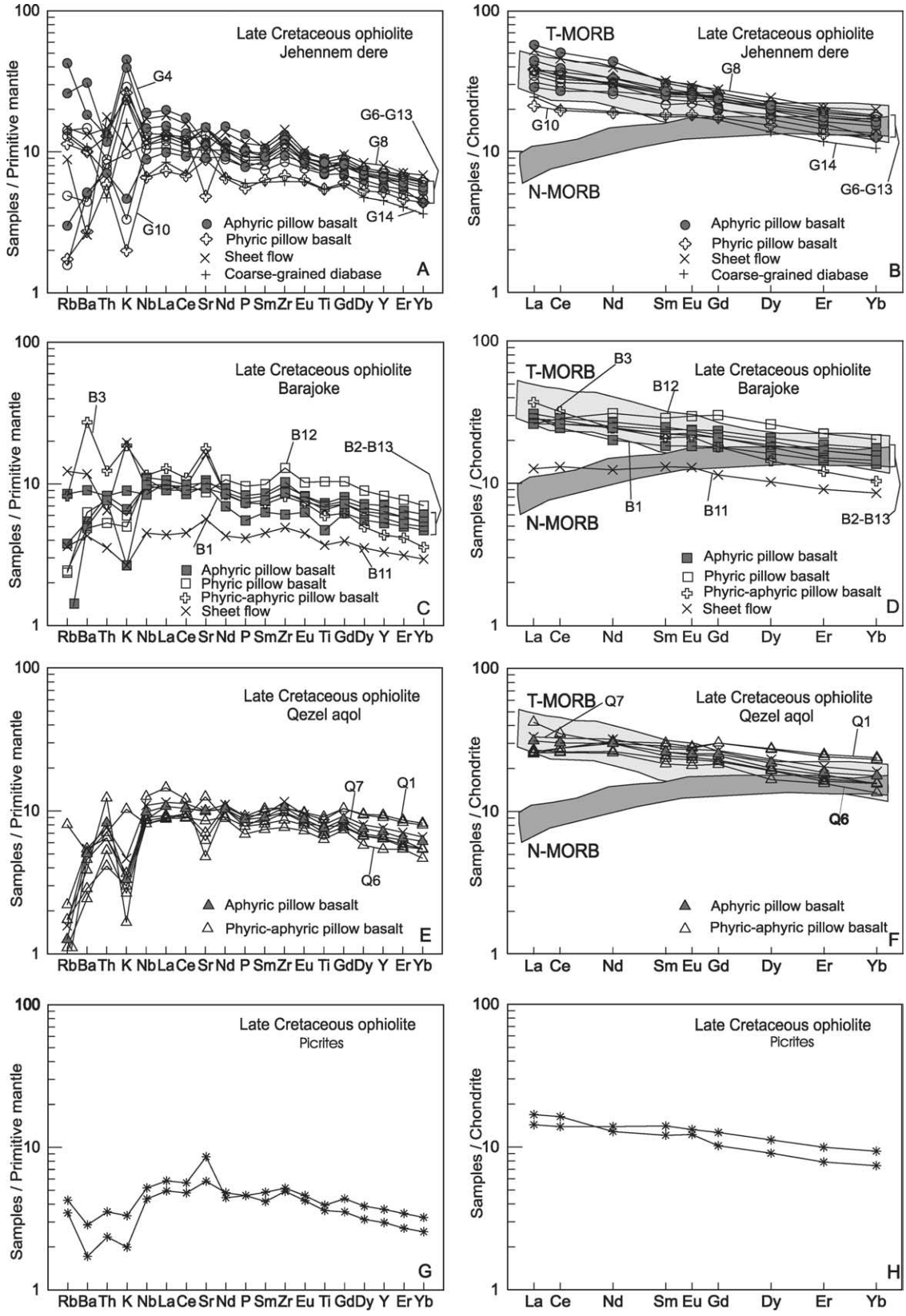

Fig. 12. Multi-element spiderdiagrams and REE profiles for the ophiolitic basalts and picrites of the southern volcanic massif. Normalizations according to Sun and Macdounough (1989).

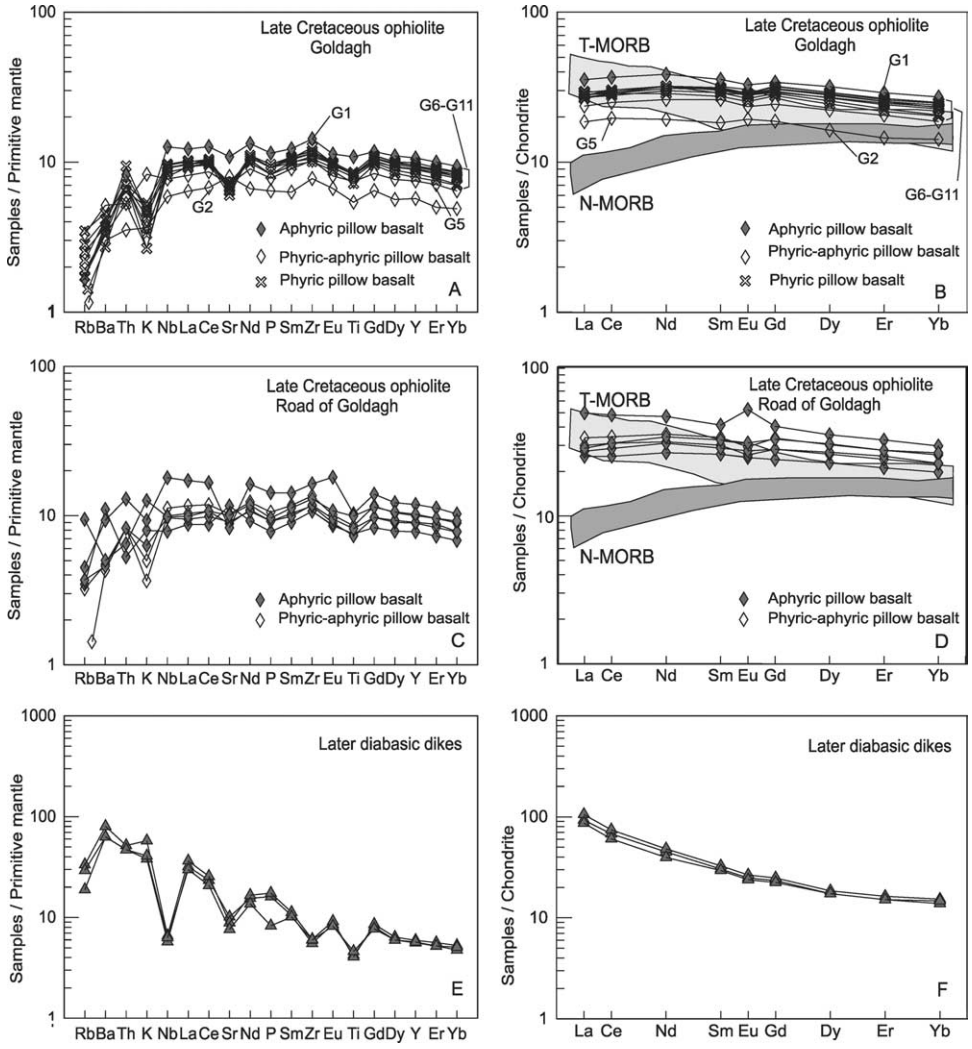

Fig. 13. Multi-element spiderdiagrams and REE profiles for the ophiolitic basalts and the late intrusive diabases of the northern volcanic massif. Normalizations according to Sun and Macdounough (1989).

turbidites plot in the basaltic trachy-andesite, trachy-andesite and basaltic–andesite fields ($51.7 < SiO_2 < 59.5\%$), and the ankaramites plot in the basaltic trachy-andesite field ($52.6 < SiO_2 < 53.7\%$).

The Ni contents are mostly < 100 ppm. The Mg# and TiO_2 contents show wide variations in the different groups: (1) from 29 to 60 and 1.8 to 2.6, respectively, in volcanic fragments reworked in the turbidites, (2) from 48 to 60 and 0.5 to 1.6, respectively, in volcanic fragments bearing a negative Nb-anomaly, (3) from 39 to 65 and 1.0 to 2.1 in pillow basalts, and (4) from 53 to 61 and 0.2 to 0.7 in the ankaramites.

Volcanic fragments without negative Nb anomalies show very homogeneous and similar trends in the multi-element plots and REE profiles (Fig. 17G). Although these lava fragments were reworked in turbidites and consequently rather deeply altered, their multi-element plots show that incompatible elements, except Rb, Ba, Th, K and Sr, remained rather immobile throughout the alteration processes. Their REE profiles are T-MORB type (Fig. 17H), very close to those of the ophiolitic lavas, with (La/Sm)N = 1.2–2.0, and (La/Yb)N = 2–3.9.

We suggest that these generally angular basaltic fragments were reworked from the Late Cretaceous ophiolitic basalts.

Volcanic fragments showing a negative Nb anomaly are characterized by flat patterns and a clear negative Nb-anomaly (Fig. 17E). The variable contents in Rb, Sr, Ba and K and their dispersion may be related to the high degree of alteration generally displayed by these samples. This group shows clearly the Nb anomaly observed in present-day 'supra-subduction' arc volcanism (Saunders and Tarnay, 1984; Hawkins and Melchior, 1985; Hofmann, 1988; Ringwood, 1990; McCulloch and Gamble, 1991; Arculus, 1994; Hawkins and Allen, 1994; Ringwood, 1990; Maury, 1993; Juteau and Maury, 1999; Pefander et al., 2002). In the REE profiles, (La/Sm)N = 1.1–2.0, and (LA/Yb)N = 1.2–1.7 (Fig. 17F).

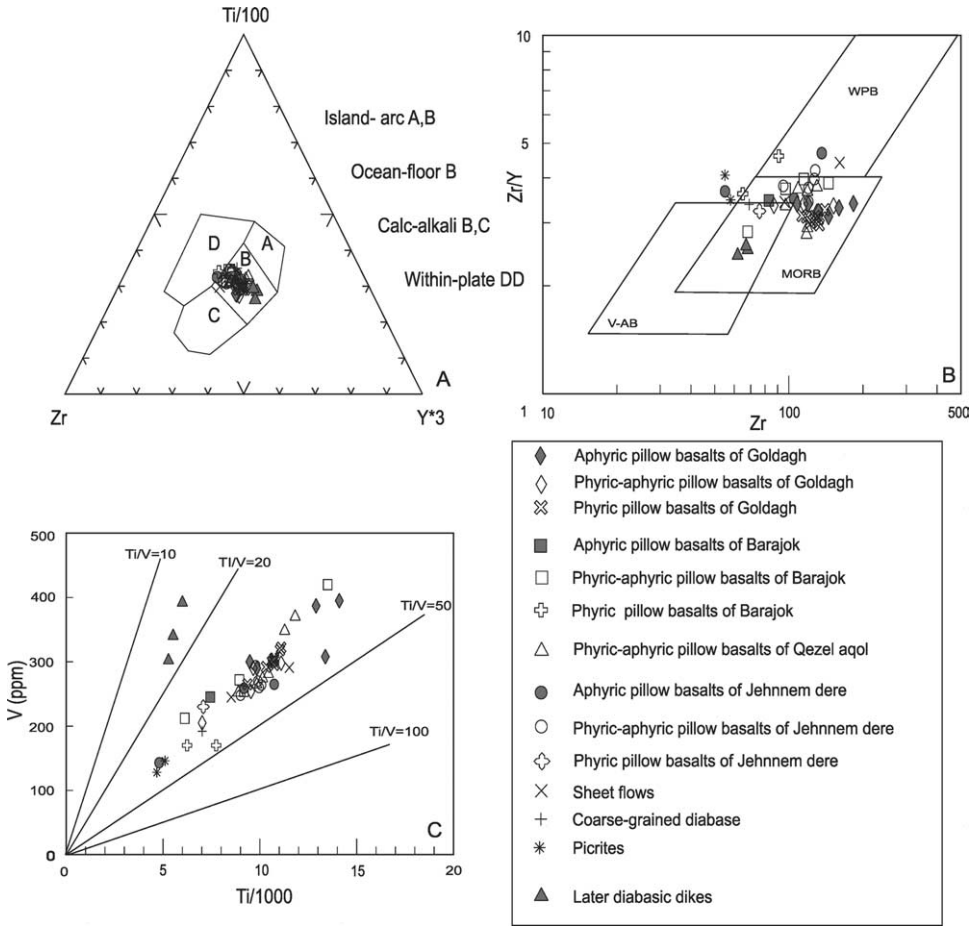

Fig. 14. Plots of the ophiolitic basalts and late intrusive diabases in some well-known tetonomagmatic diagrams, proposed by (A) Pearce and Cann (1973); (B) Pearce and Norry (1979); (C) Shervais (1982).

The significant geochemical differences between both kinds of volcanoclastic fragments in the turbidites imply *two different sources for these reworked fragments:* (a) the similarity between the first group and the pillow basalts of the Late Cretaceous Khoy ophiolite suggests that these elements were reworked from the oceanic crust outcropping to the west of the subduction trench, probably through the mass-debris flows and avalanche breccias marking the transition between the top of the pillow lava sequence and the turbidites; (b) the second group of volcanoclastic fragments, characterized by Nb negative anomalies in the multi-element plots, suggests a 'supra-subduction' origin, hence an arc-type volcanic source located to the east of the trench, along the Central Iran Block margin.

Above the turbidites and below the ankaramitic breccias, a thick unit of *pillow lava flows* is clearly visible, particularly in the Jehennem Dere valley where we sampled it. The pillows, including aphyric and phyric basalt types, are severely tectonized and altered. Their multi-element plots and REE profiles are extremely flat (Fig. 17C and D), with irregularities for several elements such as K, Sr, Ti, probably due to alteration processes. REE profiles are regular however, one of them close to an N-MORB pattern, the other ones close to T-MORB patterns very similar to those shown by the ophiolitic lavas, with (La/Sm) = 0.9–3.2, and (La/Yb) = 1.0–1.8.

The *ankaramitic breccias*, characterized by huge and abundant clinopyroxene phenocrysts, show specific multi-element plots and REE profiles with a pronounced positive slope towards LREE, and negative anomalies for K, Nb and Ti (Fig. 17A and B).

In the Zr/Y versus Y diagram, we observe a wide distribution of the sample plots (Fig. 18A). The low-Nb bearing volcanic fragments in the turbidites plot in the volcanic-arc basalts (V-AB) and MORB domains. The volcanic fragments in the turbidites plot between the mid-ocean ridge basalts and the within-plate basalts. One sample of ankaramite plots between the MORB and WPB fields, and another plots in the within-plate basalts field. The pillow basalts plot in the MORB field and out of the diagram, which indicate their wide range of chemical composition and chemical heterogeneity.

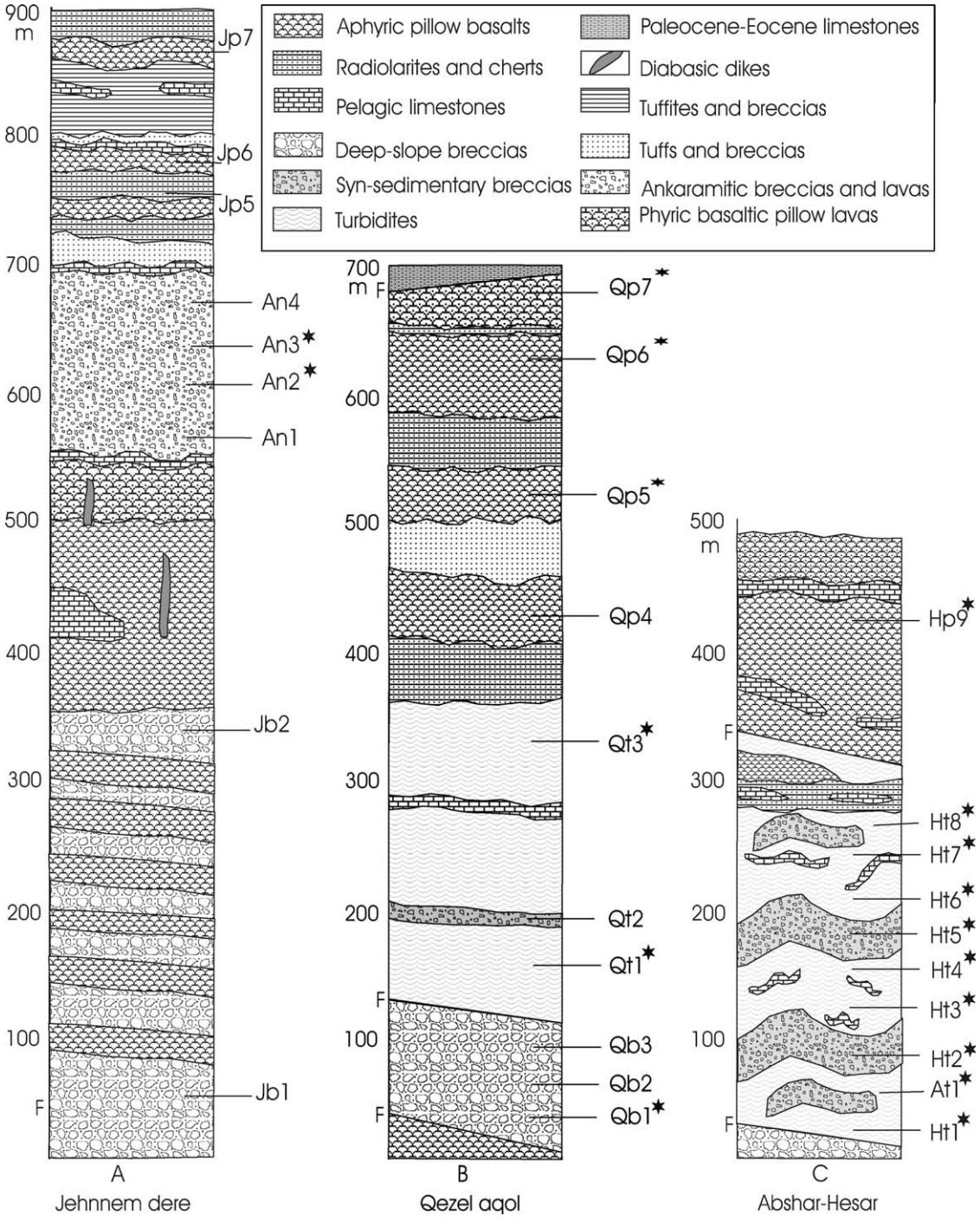

Fig. 15. Synthetic logs of the three geological sections made in the supra-ophiolitic complex of Khoy, and location of the analyzed samples (Table 3).

The V versus Ti/1000 diagram also shows a wide dispersion (Fig. 18B). However, there is a clear twofold distribution of the plots: (1) the basaltic pillow lavas and the basaltic volcanoclastic fragments in turbidites plot to the right, almost all of them in the MORB field (two of them having Ti/V > 50); (2) the low-Nb volcanoclastic fragments in turbidites and the ankaramitic lavas plot to the left in the 'supra-subduction' arc-volcanism field (Ti/V < 20).

4. The eastern metamorphic complex and associated meta-ophiolites: petrographic description and geochemistry

The eastern metamorphic complex of Khoy is essentially composed of four metamorphic units that we described in a previous paper as *m1*, *m2*, *m3*, and *m4*, respectively (Khalatbari-Jafari et al., 2004). In addition it contains huge *meta-ophiolitic tectonic slices* composed of serpentinized

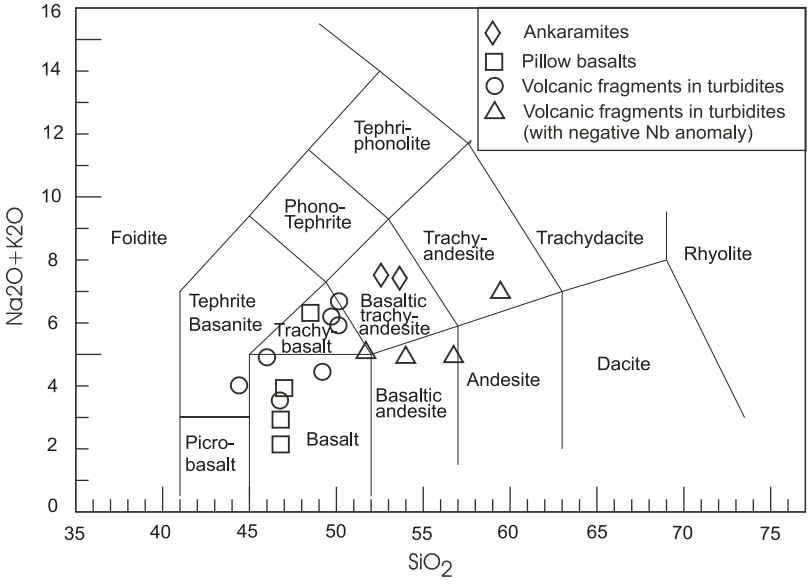

Fig. 16. Plots of the lavas of the supra-ophiolitic complex in the (Na_2O+K_2O) vs SiO_2 diagram (Le Bas et al., 1986).

lherzholites, cpx-bearing harzburgites, cumulate lherzholites and dunites, chromitites, pyroxenite veins, metagabbros and metadiabase dikes. We interpreted these metamorphic rocks, whose ^{40}K–^{40}Ar ages range from Early Jurassic to early Cretaceous, as a subduction complex tectonically underplated below the Central Iran Block margin during most of the Mesozoic (Khalatbari-Jafari et al., 2004).

4.1. The meta-ophiolitic complex

Residual mantle rocks (tectonites) are generally very serpentinized and schistosed. All the gabbroic intrusions and dikes within are completely recrystallized to amphibolites or flaser-gabbros. However in the core of the largest ultramafic massif in Susuz mountain and along the Ajai river, we found the freshest facies having escaped subsequent regional metamorphism. These samples exhibit spectacular high-temperature plastic deformations (foliations, lineations), and porphyroclastic to blastomylonitic textures typical of *mantle tectonites* (Fig. 22D and E). Whole-rock analyses of these rocks are given in Table 4.

Olivine and orthopyroxene porphyroclasts are either stretched, reaching extreme morphological ratios (length/width > 20–25), or rounded and bent within a finely recrystallized corona. Stretched olivine crystals are affected by dense kink-bands (with kink-band boundaries normal to intra-crystalline slip planes). Stretched orthopyroxene crystals have very fine cpx lamellae exsolved in the (100) cleavage planes (parallel to the slip plane). Rounded orthopyroxene crystals are bent, and exhibit mechanical kink-bands (with kink-band boundaries normal to (100) slip planes). These rocks always contain some clinopyroxene porphyroclasts, which do not deform easily and are generally deformed by rotation in the matrix. The finely recrystallized groundmass is composed of olivine, opx, cpx and disseminated Cr-spinel grains, with recrystallized olivine commonly showing triple junctions.

Olivine porphyroclasts have typical residual mantle forsteritic compositions (Fo89.7–90.6), identical to the finely recrystallized olivines of the groundmass. Clinopyroxene porphyroclasts have a diopsidic composition (Wo50Fs3En47) in the core and (Wo47Fs4En49) in the margin, with the same compositions as the tiny cpx crystals in the recrystallized groundmass. Orthopyroxene porphyroclasts have enstatite compositions (Wo5Fs9En86 to Wo2Fs9En88), while Cr-spinel compositions are variable (Cr# = 16.8–31.4, Cr_2O_3 = 15.3–24.1). Metamorphic amphiboles (Mg-rich hornblende and actinolitic hornblende) develop in numerous shear-zones, generally oriented north–south.

Cumulative meta-dunites, meta-wehrlites, meta-lherzolites and chromitites are exposed as small intrusive bodies and dikes. They have granular to mosaic textures, devoid of any evidence of high-temperature plastic deformation. They are strongly affected by serpentinization and by the development of metamorphic Mg-rich amphiboles (tremolite–actinolite). Residual olivines in the serpentine mesh have an average composition of (Fo89).

In these meta-wehrltic and meta-lherzolitic cumulates, clinopyroxene has diopsidic compositions (Wo47Fs6En47), and the cores of bastitized orthopyroxene crystals have enstatite compositions (Wo2Fs8En90). Accessory Cr-sinel crystals are oxidized to maghemite. To the northwest of Ravand village, coarse-grained cumulative meta-lherzolites outcrop and contain abundant metamorphic amphiboles ranging in composition from Mg-rich hornblende to ferropargasitic hornblende.

Chromitites form rare small podiform bodies with nodular or massive texture in a serpentinite host-rock. The

Table 3
Representative whole-rock analyses of samples from the supra-ophiolitic complex of Khoy (Late Cretaceous–Early Paleocene)

Sample	An2	An3	At1	Qt1	Qt3	Qp5	Qp6	Qp7	Ht1	Ht2	Ht3	Ht4	Ht5	Ht6	Ht7	Ht8	Hp9
Group	ank	ank	re-LNb	ae-LNb	re-NNb	pp	pp	pp	re-NNb	re-NNb	re-NNb	re-NNb	re-NNb	re-LNb	re-LNb	re-NNb	pp
SiO_2	52.6	53.7	54	59.45	46.75	46.8	46.8	47	50.15	50	50.5	44.4	46	51.7	56.75	49.2	48.65
TiO_2	0.2	0.68	0.56	1.11	1.93	1.05	1.06	1.1	2.52	2.26	2.14	1.92	2.52	1.6	1.07	1.8	2.04
Al_2O_3	16.7	15.45	15.52	13.75	15.5	16	21	18.7	13.7	13.35	14.21	13.85	14	13.1	14.05	15.2	16.5
Fe_2O_3t	8.7	7.5	9.26	8.3	11.6	10.1	7.8	9.75	12.67	10.35	11.4	9.37	8.9	9.7	9.55	10.25	12.67
FeO	6.66	5.74	7.08	6.35	8.87	7.73	5.97	7.46	9.69	7.92	8.72	7.17	6.81	7.42	7.31	7.84	9.69
Fe_2O_3	1.31	1.13	1.39	1.25	1.74	1.52	1.17	1.46	1.9	1.55	1.71	1.41	1.34	1.46	1.43	1.54	1.9
MnO	0.12	0.11	0.13	0.33	0.39	0.16	0.11	0.15	0.14	0.25	0.49	0.39	0.37	0.46	0.22	0.26	0.18
MgO	4.32	4.98	6.03	3.32	7.48	7.95	7.05	5.9	2.26	5.01	5.39	5.16	4.35	5.15	4.4	6.72	3.52
CaO	6.85	7.9	6.88	3.8	8.85	13.05	11.6	11.4	7.9	8.76	6.8	14	12.55	7.95	5.5	8.8	6.27
Na_2O	5.86	6.38	4.55	6.48	3	2.06	2.54	3.8	6.51	5.4	5.13	2.77	4.3	4.42	3.95	3.83	4.94
K_2O	1.3	0.57	0.35	0.48	0.54	0.08	0.39	0.13	0.18	0.51	0.52	1.25	0.61	0.63	0.97	0.62	1.15
P_2O_5	0.69	0.43	0.07	0.1	0.24	0.11	0.14	0.11	0.42	0.33	0.31	0.33	0.37	0.26	0.1	0.21	0.62
LOI	2.24	1.98	2.13	2.67	3.33	2.36	1.05	2.71	2.86	3.34	2.58	5.96	5.92	4.82	3.7	3.16	3.33
Total	100.18	99.68	99.48	99.79	99.61	99.72	99.54	99.95	99.31	99.56	99.47	99.4	99.89	99.79	100.2	100.05	99.87
Mg#	53.65	60.75	60.28	48.25	60	64.7	67.8	58.5	29.36	53	52.42	56.2	53.25	55.3	51.78	60.45	39.3
Rb	25	7.5	5.1	5	9.2	1.5	4.9	1.6	2.8	9.1	6.3	22.5	5.6	8.4	9.2	6.8	10
Ba	250	330	23	52	66	25	86	21	44	49	120	103	98	63	83	104	156
Th	10.5	11.3	0.3	0.5	1	0.45	0.65	0.3	1.45	1.4	3.35	1.05	1.7	0.9	0.45	1.05	2.65
K	10790	4731	2905	3984	4482	664	3237	1079	1494	4233	4316	10375	5063	5229	8051	5146	9545
Nb	50	56	1.6	3.7	9	4	8.5	2.7	17	17.5	22.5	13.3	16	6.9	3.1	8.9	28
La	107	88	4	4.5	10.3	5.2	7.2	3.1	19	16	15.5	13.5	16.5	8.9	4.3	8.2	26
Ce	208	157	6.8	10	26	11.4	16.5	8.8	40	37.5	37	32	41	22.5	10.3	21	61
Sr	905	760	190	189	194	163	339	251	80	352	522	286	268	133	215	308	183
Nd	17	54	3.4	7.5	18	8.2	9.6	7.7	25.5	23	23	21	27	15	7.65	14.5	39
Sm	12.4	9	1.3	2.4	5	2.55	2.55	2.7	6.2	5.6	5.8	5.1	6.75	4.2	2.55	4.25	9.5
Zr	119	183	23	57	141	63	73	70	189	183	186	145	205	124	57	128	308
Eu	3.41	2.47	0.54	0.95	1.78	1	0.94	1.05	2.15	1.91	2.05	1.76	2.35	1.45	0.95	1.53	2.95
Ti	1200	4080	3360	6660	11580	6300	6360	6600	15120	13560	12840	11520	15120	9600	6420	10800	12240
Gd	8.7	6.5	1.7	3	6.1	3.5	2.8	3.3	7.4	6.2	6.8	5.6	8.45	5.25	3	4.75	10.6
Dy	5.45	4.55	2.4	3.95	6.75	3.9	2.7	4.15	7.3	5.95	7.3	5.6	8.15	6.45	3.95	5.3	10.5
Y	30.5	26	15.5	23.5	42	23.5	15.2	25	46.5	33	48	33.5	51	38.5	25	31.5	61
Er	2.7	2.3	1.7	2.35	4.1	2.3	1.4	2.5	4.4	3.15	4.6	3	4.6	3.8	2.5	2.9	6
Yb	2.45	2.09	1.7	2.34	3.75	2.35	1.3	2.41	3.9	2.95	4.35	2.6	4.1	3.76	2.55	2.68	5.75
Sc	9	21	36	35	40	37	28	34	27	34	35	33	31.5	37	32	36	19
V	170	200	285	380	265	240	172	218	322	290	335	250	251	292	328	248	160
Cr	22	255	31	4.5	133	300	120	244	39	87	15	170	23	18	4	168	29
Co	24	27	31	30	41	42	35	43	22	29	40	26	31	40	29	54	29
Ni	28	77	54	27	110	120	59	83	22	36	80	58	45	52	26	102	16
(La/Yb)N	31.33	30.2	1.69	1.38	1.97	1.59	3.97	0.92	3.49	3.89	2.56	3.72	2.89	1.7	1.21	2.19	3.24
(La/Sm)N	0.07	0.06	0.02	0.03	0.03	0.03	0.04	0.03	0.03	0.04	0.03	0.03	0.03	0.02	0.02	0.03	0.03
Zr/Nb	0.02	0.01	0.07	0.04	0.03	0.04	0.02	0.04	0.02	0.02	0.02	0.02	0.02	0.03	0.04	0.02	0.02
Ce/Yb	84.9	75.12	4	4.27	6.93	4.85	12.69	3.65	10.26	12.71	8.51	12.31	10	5.98	4.04	7.84	10.61

Sample symbols: An, ankaramitic lava unit; Qt, turbidites from Qezel Aqol section; Qp, supra-ophiolitic pillow lavas from Qezl Aqol section; Ht, turbidites from Hesar-Abshar; Hp, pillow basalt of Hesar. Group symbols: re-Lnb, rounded volcanic fragments, with Nb negative anomaly; re-NNb, rounded volcanic fragments, without negative Nb anomaly; ae-LNb, angular volcanic fragments, with Nb negative anomaly; ank, ankaramitic basalts; pp, phyric pillow lavas.

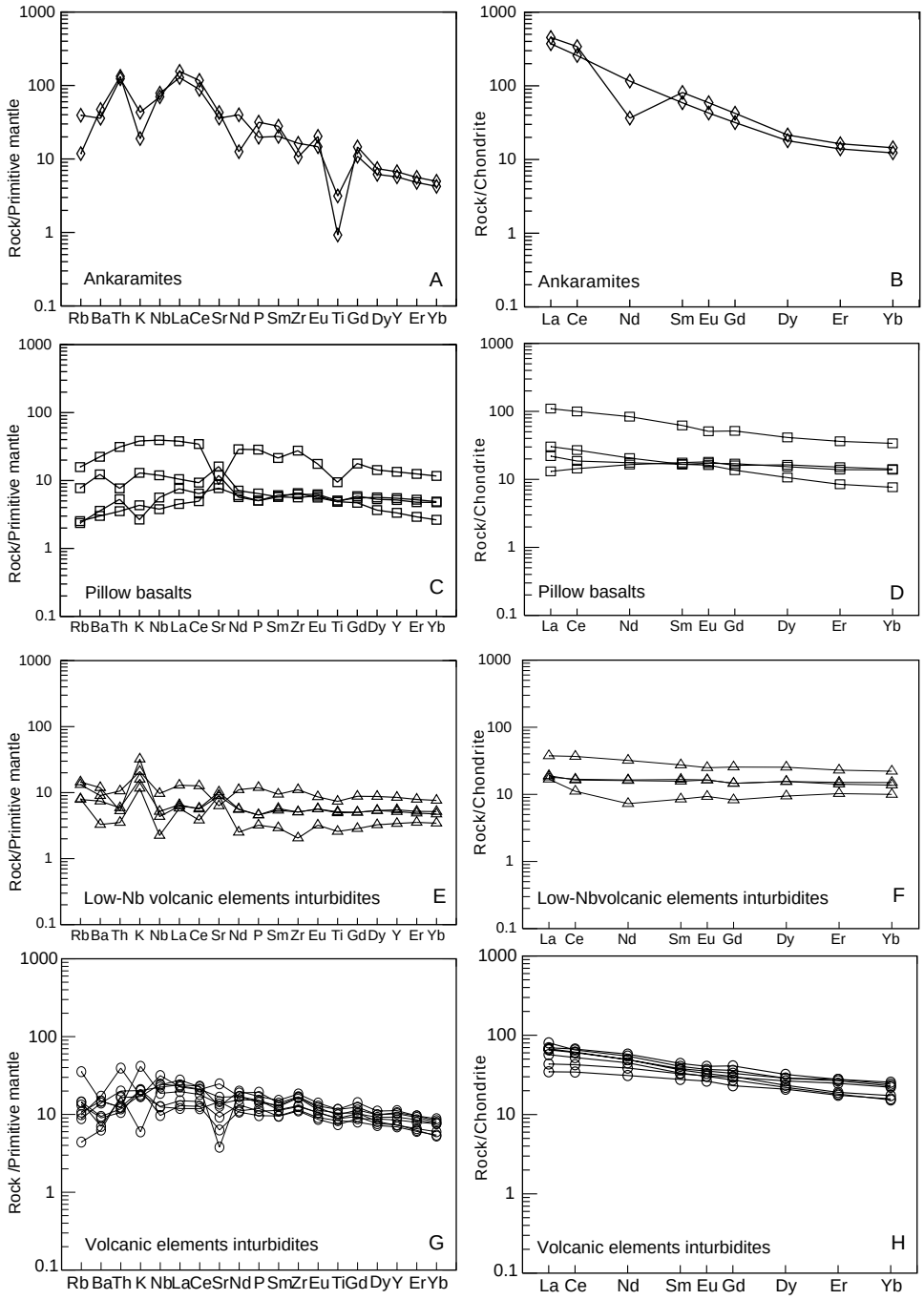

Fig. 17. Multi-element spiderdiagrams and REE profiles for the lavas of the supra-ophiolitic complex. Normalizations according to Sun and Macdounough (1989).

Cr# of the chromite grains ranges between 47 and 64, with $Cr_2O_3 = 39–40\%$.

Coarse-grained meta-gabbros are nicely foliated and essentially made of banded amphibolites (Fig. 22F), with alternating amphibole-rich layers (magnesian-hornblende to pargasitic hornblende) and plagioclase-rich layers (An76–30). Relics of deformed and rotated clinopyroxene crystals (Wo33Fs22En45–Wo47Fs6En47) are completely replaced by amphiboles.

Whole-rock analyses of these metagabbros are given in Table 5. The multi-element plots (Fig. 19A) show a wide compositional dispersion that is difficult to interpret. Obviously, the hydration accompanying metamorphic recrystallization has favoured the mobility of many trace elements in these rocks. The REE patterns of the metagabbros (Fig. 19B) are more regular and can be subdivided into three types of profiles: (a) flat profiles, slightly above 10 times that of chondrites, which may represent T-MORB-type liquids (isotropic gabbros); (b) LREE-depleted profiles (from 4 to 20 times chondrites), that may represent N-MORB-type liquids (isotropic gabbros); (c) depleted profiles with clear positive Eu

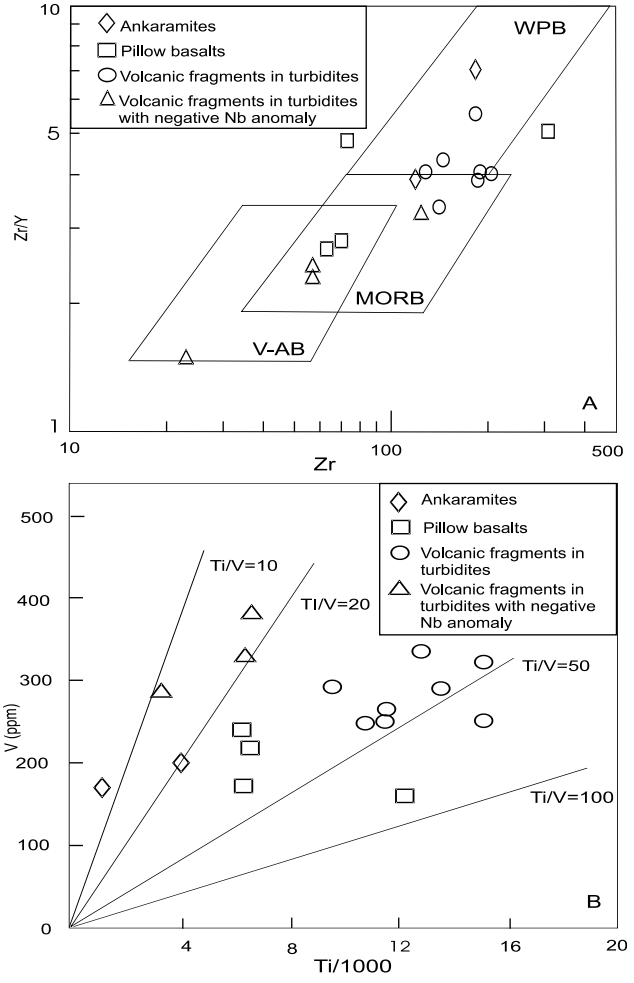

Fig. 18. Plots of the lavas of the supra-ophiolitic complex in two tetonomagmatic diagrams, proposed by: (A) Pearce and Norry (1979), and (B) Shervais (1982).

anomalies, probably representing plagioclase-rich gabbroic cumulates.

4.2. Metamorphic rocks of the eastern metamorphic complex

Table 6 gives some whole-rock analyses of these rocks, including some of the Cretaceous granitic intrusions crosscutting them.

The m1 metamorphic unit is composed of amphibolites and micaschists at the base, followed by marbles, quartzites and extended gneiss (Fig. 22G). The finely crystallized *amphibolites* are composed of hornblende, fine plagioclase laths (An36) and fine-grained quartz and magnetite (Fig. 22H). The *gneissses* are made of coarse and rotated plagioclase phenoblasts (showing 'pressure shadow' features), commonly replaced by albite (An6), orthoclase and sericite. Large quartz phenoblasts are also rotated and deformed in a fine-grained and recrystallized matrix composed of quartz, plagioclase and muscovite (mortar textures, evolving by places toward mylonitic textures). The *micashists* are characterised by coarse-grained biotite-rich bands, alternating with fine-grained bands rich in muscovite, quartz and plagioclase (An16). *Quartzites* and *marbles* show mosaic textures with well recrystallized minerals.

Multi-element plots and REE profiles of one *m1* amphibolite sample and one gneiss sample are showed in Fig. 19G and H. These patterns showing a weak dispersion are enriched in LILE and LREE, with negative anomalies in Sr and Ti. In addition, the amphibolite shows small negative anomalies for Nb and Ti. The negative Sr anomaly can be related to alteration of K-bearing minerals. The REE patterns are regular (except for an Eu negative anomaly in

Table 4
Representative whole-rock analyses of samples from the meta-ophiolitic complex, ultramafic rocks (eastern metamorphic complex of Khoy)

Sample	Mu1	Mu2	Mu3	Mu5	Mu8	Mu12	Mu13	Mu14
SiO_2	42.5	42.5	41.6	38	39.5	41.5	40	42.2
TiO_2	0.022	0.045	0.025	0.02	0.043	0.014	0.014	0.015
Al_2O3	1.66	1.48	1.5	1.05	1.31	0.87	1.12	1.26
Fe_2O3	8.6	9.3	8.7	9.55	9.1	9.2	9.3	8.9
MnO	0.12	0.135	0.12	0.135	0.13	0.13	0.13	0.13
MgO	41.2	42	42	43.3	42.4	44.3	44	42
CaO	1.75	1.85	1.6	0.97	0.85	0.87	1.18	2.05
Na_2O	0.05	0.07	0.045	0.07	0.035	0.04	0.036	0.035
K_2O	0.025	0.003	0.002	0.003	0.004	0.001	0.004	0.008
P_2O5	0.014	0.018	0.014	0.02	0.016	0.016	0.017	0.017
LOI	2.94	2.1	3.28	6.56	5.69	2.11	1.5	2.37
Total	99.88	99.08	98.89	99.68	99.08	99.05	99.3	99
Ba	0	0.5	0.5	1	1.5	0.5	0.5	0.5
Sr	1.3	1.5	1.6	3	1.5	0.7	1	1.3
Zr	2.5	3	3	2.5	2.5	2.5	2	2
Sc	11.6	12	11	8	10	8.5	10.3	12
V	51	57	49	36	45	37	49	58
Cr	2150	2350	2360	2300	2500	1700	2050	2450
Co	100	110	105	120	110	109	120	110
Ni	2000	2250	2080	2250	2200	2250	2400	2250

Table 5
Representative whole-rock analyses of samples from the meta-ophiolitic complex, metagabbros (eastern metamorphic complex of Khoy)

Sample	Mg2	Mg3	Mg4	Mg5	Mg6	Mg8	Mg12
SiO_2	41.6	44.7	49.65	42.5	44	42.7	48.7
TiO_2	2.07	1.32	0.25	1.67	0.86	1.51	0.2
Al_2O_3	12.8	12	17.35	14.96	12.55	12.3	18.9
Fe_2O_3	14.05	10.72	6.55	13.56	7.3	15.4	6.4
MnO	0.23	0.15	0.13	0.23	0.07	0.19	0.11
MgO	13.65	15.45	8.55	10.15	17.75	11.75	8.9
CaO	11	11.5	13	12.6	12.4	11.65	12.1
Na_2O	2.5	2.4	3.18	1.58	2	2.1	2.28
K_2O	0.08	0.07	0.05	0.17	0.25	0.19	0.39
P_2O5	0.27	0.03	0.02	0.07	0.02	0.04	0.02
LOI	1.48	1.25	1.51	1.74	2.7	1.28	2.15
Total	99.73	99.59	100.24	99.23	99.9	99.11	100.15
Rb	0.2	0.4	0.35	0.4	0.6	1.5	12.3
Ba	7	7	11	19	8	34	86
Th	0.25	0.15	0.1	0.15	0.2	0.2	0.1
Nb	5.1	1.5	0.3	9.1	1.8	1	0.6
La	5.9	1	0.55	4.2	1.4	0.6	0.7
Ce	18.5	3.5	1	14.5	4	1.5	1.2
Sr	72	44	200	139	44	18	152
Nd	18	6	0.9	14	5.3	1	0.7
Sm	6.1	2.6	0.45	4.1	2.05	0.7	0.5
Zr	105	25	7.5	58	19	7	6
Eu	2.08	1.02	0.45	1.36	0.64	0.45	0.38
Gd	9.25	4	1	5.1	2.65	1	0.9
Dy	11	5.3	1.35	5.75	2.6	1.3	0.9
Y	68	31.5	7.8	33	15	8.5	5.3
Er	6.7	3	0.8	3.3	1.5	0.9	0.5
Yb	6.5	2.9	0.8	3.25	1.22	0.84	0.55
Sc	37	47	38	41	59	49	31
V	335	270	150	395	450	950	135
Cr	250	1225	335	560	725	85	215
Co	56	60	38	55	72	68	38
Ni	215	640	108	265	540	170	70

the gneiss sample) and high in the diagram, showing a slight decrease from LREE to HREE.

The m2 metamorphic unit is essentially made of fine-grained amphibolites, accompanied by greenschists, micas-chists, quartzites and gneiss. Incipient partial melting has affected this series in places. The amphibolites consist of amphibole and plagioclase with a wide compositional range, from oligoclase to bytownite (An24–84). Small relics of diopsidic clinopyroxene are visible in the groundmass, made of chlorite, epidote and sericite. These fine-grained amphibolites are interbedded with greenschists and marbles, suggesting a submarine volcanic origin.

Intrusive diabases dikes recrystallized to amphibolites contain some relics of clinopyroxene, replaced by fine-grained hornblende and tremolite–actinolite. The plagioclase laths are zoned and albitized. Sphene, epidote, calcite and abundant chlorite are secondary minerals.

The greenschists are composed of sericite, muscovite, chlorite, and calcite along with an abundance of boudinated and folded quartz lenses.

The multi-element plots and REE profiles of the *m2* metamorphic amphibolites have flat patterns (Fig. 19C and D). The multi-element plots show strong variations in the LILE (Rb, Ba, Th, K), and pronounced negative anomalies in Zr. Nb and Ti are variable, with poorly-defined negative anomalies. The flat REE patterns show a slight enrichment in LREE (10–25 times chondrites).

The association of these fine-grained amphibolites with greenschists acompanied by red meta-radiolarites, calcs-chists and limestones in the *m2* unit, suggests a volcanic origin for these amphibolites. Moreover, they could represent the extrusive sequence of the meta-ophiolitic complex. Arguments in favour of this hypothesis are: (a) the similarity of REE profiles of some metagabbros with the *m2* amphibolites (compare the highest profiles in Fig. 19B with those of Fig. 19D); (b) similarity of K–Ar ages (Early Jurassic to Early Cretaceous) obtained on both formations (Khalatbari-Jafari et al., 2004); (c) the systematic tectonic juxtaposition of both formations in the field, suggesting that there was originally a narrow link between them.

4.2.1. The crosscutting granite

In the vicinity of Ajidgah village, the *m2* amphibolites are crosscut by an intrusive granite, and both units are

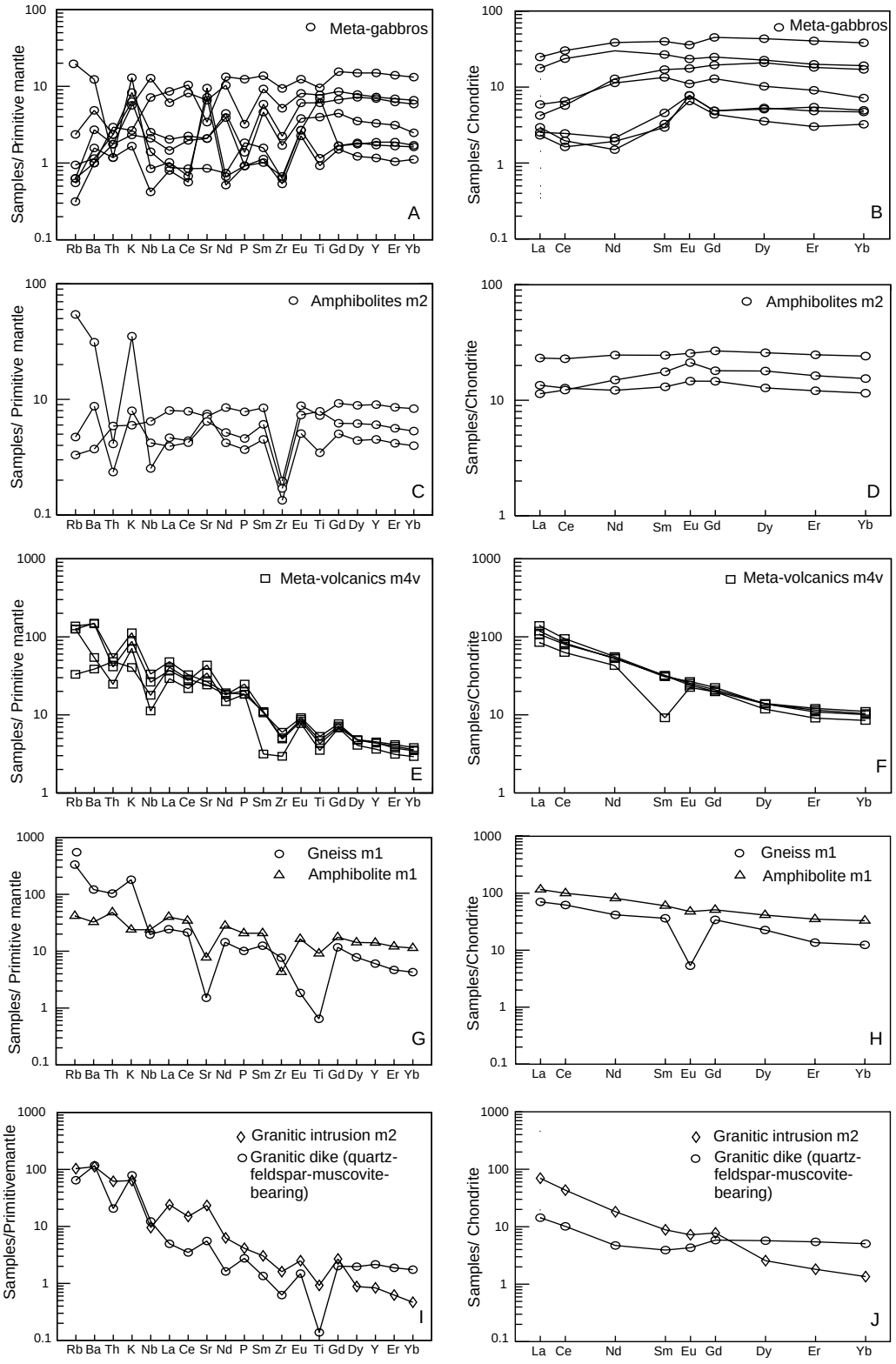

Fig. 19. Multi-element spiderdiagrams and REE profiles for the meta-ophiolitic gabbros, metamorphic rocks and intrusive granites from the eastern metamorphic complex of Khoy. Normalizations according to Sun and Macdounough (1989).

Table 6
Representative whole-rock analyses of samples from the esatern metamorphic complex of Khoy, and associated granitic intrusions

Unit	m1	m2	m2	m2	m2	m2	m2	m4	m4	m4	m4
Sample	Mt1	Mt2	Mt7	Mt8	Mt11	Mt12	Mt13	Mv1	Mv2	Mv3	Mv4
Rock-type	amp	gne	amp	amp	amp	QFdyke	gr	mt-v	mt-v	mt-v	mt-v
$TSiO_2$	54.5	77.2	47.1	48.4	48.6	75	71.3	49.35	47.8	49.2	47.15
TiO_2	1.97	0.14	0.75	1.57	1.71	0.03	0.2	0.76	0.93	1.02	1.15
Al_2O_3	14.05	11.75	16.63	14.42	13.75	14.03	15.95	12.45	16.5	17	16.45
Fe_2O_3	13.1	1.72	9.7	12.47	13.8	0.63	1.64	10	9.18	8.9	10.26
MnO	0.22	0.02	0.17	0.2	0.21	0.06	0.04	0.18	0.18	0.15	0.18
MgO	3.98	0.1	0.37	7.12	7.1	0.16	0.71	7.7	7.66	3.18	5.75
CaO	7.7	0.6	10.35	10.2	10.5	1	2.96	12.8	8.86	9	9.6
Na_2O	2.11	1.74	2.23	3	2.94	4.92	4.38	1.77	2.03	5.38	2.44
K_2O	0.72	5.45	1.06	0.18	0.24	2.37	1.92	2.14	3.39	1.22	2.63
P_2O_5	0.45	0.22	0.08	0.17	0.1	0.06	0.09	0.4	0.4	0.54	0.44
LOI	0.64	1.14	2.16	1.2	0.65	0.6	0.65	2.53	3.18	5.03	3.4
Total	99.44	100.08	99.6	99.33	99.6	99.15	99.84	100.08	99.51	100.62	99.45
Rb	26.5	212	34.5	2.1	3	41	65.5	80	79.5	21	87.5
Ba	227	850	218	26	61	820	780	380	1045	270	1025
Th	4.1	8.8	0.35	0.5	0.2	1.75	5.25	2.1	4.6	4.1	3.5
Nb	17	14	1.8	4.6	3	8.7	6.8	8	23.8	12.7	18.7
La	27.5	16.7	3.2	5.5	2.7	3.4	16.5	20	33	28	25.5
Ce	61	38	7.8	14	7.5	6.2	26.5	38.5	58	51	49
Sr	163	32	158	150	136	117	492	725	560	510	917
Nd	38	19.5	5.7	11.5	7	2.2	8.5	20	26	24.5	25
Sm	9.2	5.55	2	3.75	2.7	0.6	1.35	1.4	4.85	4.9	4.7
Zr	48	86	15	22	19	7	18	33	55	57	67
Eu	2.76	0.31	0.85	1.48	1.23	0.25	0.42	1.3	1.39	1.47	1.55
Gd	10.5	7	3	5.5	3.7	1.2	1.6	4.05	4.1	4.3	4.6
Dy	10.5	5.75	3.25	6.55	4.55	1.45	0.65	3	3.5	3.55	3.5
Y	64	27.5	20.5	41	27.5	9.8	3.8	16.5	19.8	20.5	20
Er	5.8	2.25	2	4.1	2.7	0.9	0.3	1.5	1.9	2	1.8
Yb	5.6	2.11	1.96	4.1	2.62	0.86	0.23	1.44	1.76	1.88	1.71
Sc	35	7.4	31	43	49	1.5	2	47	37	19	32
V	225	5	195	330	430	4	10	300	270	330	350
Cr	116	3.5	400	200	118	3.5	5	305	137	4	45
Co	29	0.5	49	38	46	0.5	2.5	38	32	23	34
Ni	44	1.5	150	75	62	2	3	85	70	14	29

Rock-type symbols: amp, amphibolite; gne, gneiss; QFdyke, quartz-feldspar-muscovite-bearing dyke; gr, granite; mt-v, meta-volcanic rocks (meta-basalts, meta-andesites, meta-ankaramites).

intersected by numerous pegmatitic granite dikes. The granite has a granular, often mylonitic texture. Zoned plagioclase phenocrysts (An10–28) and perthitic orthoclase indicate a magmatic origin. Small muscovite and biotite crystals are abundant.

On the multi-element plots of Fig. 19I, the Ajidgah granite shows typical characteristics of arc-type orogenic granites, with moderate negative anomalies in Nb, Zr and Ti. The REE profiles (Fig. 19J) show a pronounced LREE enrichment (up to 100 times chondrites). The pegmatite dikes exhibit the same profile, but with a more depleted REE profile.

The m4 metamorphic unit is composed of schistosed metavolcanic rocks metamorphosed in the greenschist facies. These meta-andesites and metabasalts have relics of diopsidic clinopyroxene (En53Fs4En43) in the groundmass, mostly altered to epidote and chlorite. The plagioclase is replaced by albite, chlorite and calcite. We have also found some meta-ankaramitic facies containing abundant clinopyroxene phenocrysts in the altered mesostasis. These rocks sometimes contain decimetric dioritic inclusions, whose altered plagiclases are completely replaced by clay minerals and actinolitic hornblende.

The multi-element plots and REE profiles of the *m4* metavolcanic rocks are quite different from those of the other metamorphic units. The spiderdiagram (Fig. 19E) shows a pronounced positive slope toward the LILE elements and clear negative anomalies for Nb, Zr and Ti. The REE patterns (Fig. 19F) also show a steep positive slope toward the LREE (up to 100 times chondrites for La), whereas the HREE remain at much lower concentrations (10 times chondrites for Er and Yb). One of the samples shows an unexplained negative anomaly in Sm. These are typical *calc-alkaline patterns* suggesting that these lavas, before being metamorphosed, were emplaced in an arc-type, 'supra-subduction' environment.

5. General discussion

In a previous paper, we presented the new geological map and field data for the area of Khoy, accompanied by new ^{40}K–^{40}Ar and micro-paleontological datings (Khalatbari-Jafari et al., 2004). We also presented our conception of the geodynamic evolution of the region of Khoy (Khalatbari-Jafari et al., 2004, Fig. 16), and will not repeat it here. The present paper is conceived as a complementary companion-paper of the previous one. It is based on petrographic studies of thin sections, on about 3500 electron microprobe analyses of the mineral phases, and on 113 new whole-rock ICP-AES analyses (Khalatbari-Jafari, 2002).

The main conclusions of our petrological and geochemical study are summarized in the following points:

5.1. Existence of two ophiolite complexes in the Khoy area

The petrographic study of numerous thin sections confirms the field data showing the existence of two ophiolite complexes in the region of Khoy (Khalatbari-Jafari et al., 2003, 2004; Juteau, 2004), and indicate the following (see Figs. 20–22):

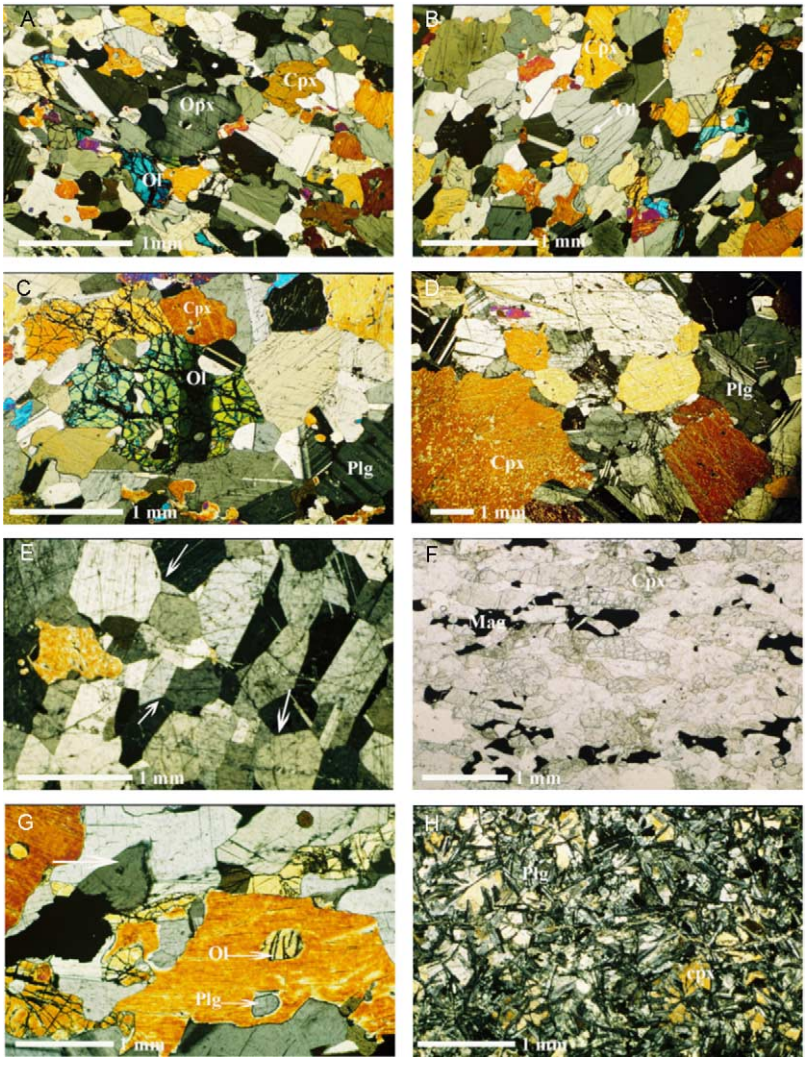

Fig. 20. Layered gabbros (Late Cretaceous ophiolite of Khoy). (A) Mosaic texture of an olivine gabbro (mesocumulate). Under crossed nichols. Sample from south of Todan village. (B) Olivine gabbro. Inclusions of small olivine crystals in clinopyroxene (arrows), under crossed nichols. Sample from south of Todan village. (C) Kink-bands in olivine gabbro, due to compaction processes in a crystal mush, under crossed nichols. Sample from south of Todan village. (D) Coarse-grained gabbronorite, showing large clinopyroxene and plagioclase crystals, with a mosaic texture, under crossed nichols. They contain orthopyroxene, but not olivine. Sample from south of Todan village. (E) Layered anorthosite, composed mostly of plagioclase (90%) and minor clinopyroxene (about 10%), under crossed nichols. Arrows show triple-junctions between plagioclase crystals. Sample from south of Todan village. (F) Ferrogabbro, at the top of the layered sequence, mainly composed of plagioclase, clinopyroxene and iron oxides (Ti–magnetite, ilmenite), under parallel nichols. Sample from south of Todan village. (G) Pegmatite-gabbro in layered gabbros, under crossed nichols. Arrows show small olivine inclusions in large clinopyroxene crystals. Sample from south of Todan village. (H) Typical intersertal texture of a diabase dike crosscutting the layered gabbros, under crossed nichols. Sample collected near Hesar village.

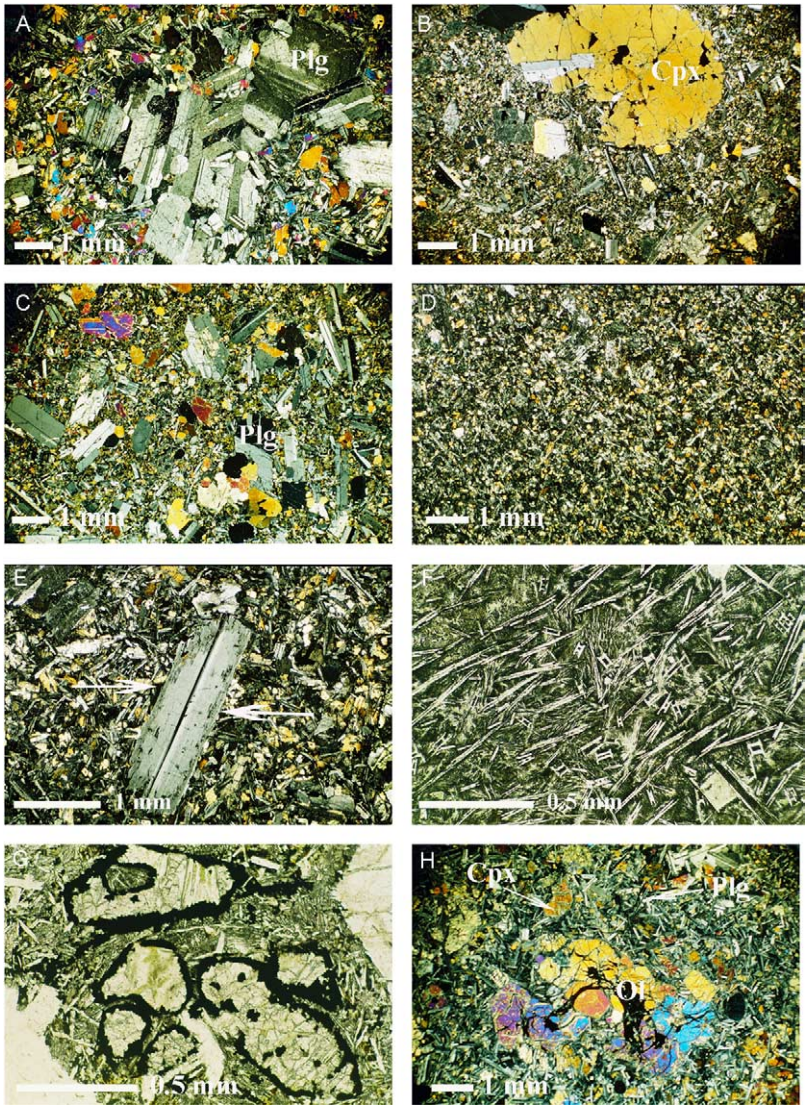

Fig. 21. The extrusive sequence (Late Cretaceous ophiolite of Khoy). (A) Megacrysts-bearing phyric basalt. Cluster of plagioclase megacrysts in a matrix containing plagioclase and clinopyroxene pheonocrysts, microphenocrysts and microlites, under crossed nichols. The rock is fresh. (Barajok section, southern volcanic massif, pillow lava flow). (B) Megacrysts-bearing phyric basalt. Clinopyroxene megacryst, including a plagioclase phenocryst, in a matrix containing plagioclase and clinopyroxene pheonocrysts, microphenocrysts and microlites, under crossed nichols (Goldagh section, northern volcanic massif, pillow lava flow). (C) General aspect of a phyric basalt, with plagioclase and clinopyroxene phenocrysts, in a matrix containing plagioclase and clinopyroxene pheonocrysts, microphenocrysts and microlites, under crossed nichols (Goldagh section, northern volcanic massif, pillow lava flow). (D) General aspect of an aphyric basalt, totally devoid of phenocrysts, and composed of plagioclase, clinopyroxene and Ti–magnetite microlites, in a devitrified groundmass, under crossed nichols (Jehennem Dere section, southern volcanic massif, pillow lava flow). (E) Corroded Ca-rich plagioclase phenocryst, with later growth of outer Na-rich layers. Arrows show small glassy inclusions at the boundary between both zones, under crossed nichols (Goldagh section). (F). Typical quenched textures (with the well-known 'belt buckles', transverse sections of hollow plagioclase microlites, and 'bifid tips' in longitudinal sections), well preserved in the margin of a basaltic pillow lava, under parallel nichols. (Jehennem Dere section). (G) Cluster of olivine phenocryst 'phantoms', entirely pseudomorphosed to chlorite, calcite, serpentine and a rim of iron oxides, under parallel nichols (Barajok section). (H) General aspect of olivine-rich picritic sill-like intrusions in the southern volcanic massif, under crossed nichols (North of Dizadj Aland village).

– The *Late Cretaceous ophiolite*, outcropping to the west of the studied area, is devoid of any trace of regional metamorphism. The gabbros are amphibole-free and exhibit delicate magmatic structures and textures, whereas the submarine basaltic lavas show unaltered or weakly altered mineral phases, and even relics of isotropic glass in the pillow margins.

– The *Early Jurassic to Early Cretaceous meta-ophiolite slices*, tectonically included in the 'eastern metamorphic complex', have a totally different aspect. They are recrystallized in the amphibolite facies, with a strong penetrative foliation. The cores of the largest slices, however, have escaped recrystallization. Porphyroclastic to mylonitic lherzolites and harzburgites exhibit high-T

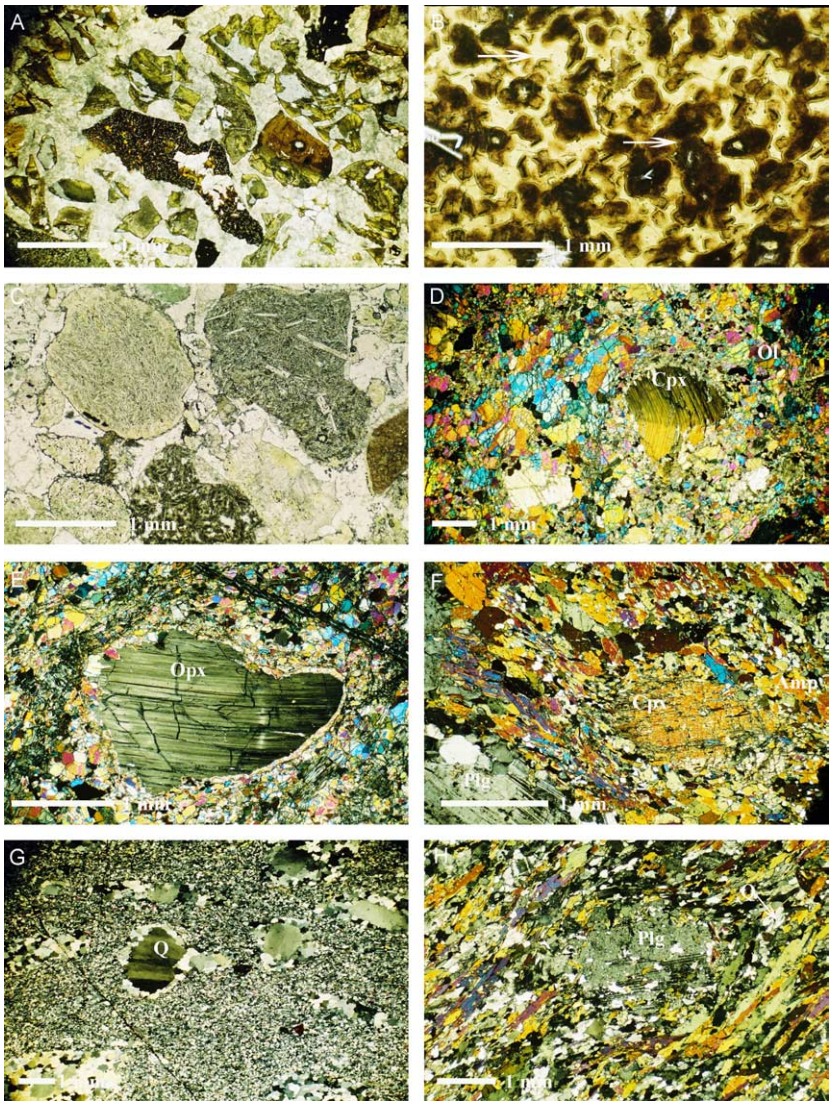

Fig. 22. Volcanic breccias, turbidites, meta-ophiolites and eastern metamorphic complex. (A) General aspect of fine-grained layered hyaloclastites in the ophiolitic extrusive sequence, made of angular devitrified glass shards, in a carbonate matrix, under parallel nichols. (Sample from the Jehennem Dere section, southern volcanic massif.) (B) Relic variolitic zone in the margin of a pillow lava, under parallel nichols. Spherical devitrification varioles develop around crystal germs, in a matrix made of yellow, isotropic glass. Micoprobe analyses of this glass showed that it is hydrated (10–15% LOI). (Sample from the Jehennem Dere section.) (C) Detail of a turbiditic layer, made of rounded volcanic fragments in a matrix made of carbonates, clays and some quartz, under parallel nichols (sample from the supra-ophiolitic turbidites, Abshar cascade). (D) Porphyroclastic lherzolite showing a deformed diopside porphyroclast with kink bands, under crossed nichols. This porphyroclast has rotated within a finely granulated olivine matrix (meta-ophiolite unit, eastern metamorphic complex, South of Aqbash village). (E) Porphyroclastic harzburgite, showing a deformed enstatite porphyroclast, with undulose extinction and bent (100) cleavages, under crossed nichols. This porphyroclast has rotated within the fine-grained, recrystallized olivine matrix (i.d. South of Aqbash village). (F) General aspect of a meta-gabbro from the meta-ophiolitic unit (eastern metamorphic complex), under crossed nichols. Relic clinopyroxene porphyroclasts are deformed and rotated in a metamorphic matrix, mainly composed of plagioclase and actinolitic hornblende (Sample from north of Khoy). (G) Mylonitic gneiss from the *m1* metamorphic unit, showing deformed quartz porphyroclasts, in a fine-grained matrix of quartz, feldspar and micas, under crossed nichols. (sample collected near Hyderabad, north of Khoy). (H) Porphyroclastic amphibolite from the *m1* metamorphic unit, showing a deformed plagioclase porphyroclast, rotated within the recrystallized matrix, under crossed nichols (sample collected near Hyderabad, north of Khoy).

deformations typical of mantle conditions (Nicolas, 1989) . Gabbroic bodies included in these peridotites are always transformed to amphibole-rich foliated metagabbros. The volcanic series are no more recognizable: we think that significant parts of the m2 fine-grained amphibolites in the ‘eastern metamorphic complex’ could represent, at least partly, a former ophiolitic extrusive sequence genetically associated with the metagabbros.

5.2. The Late Cretaceous ophiolite shows mineralogical and geochemical characteristics of a T-MORB-type tholeiitic series

The normalized multi-element plots and REE profiles of the extrusive sequence (55 analyses) are well clustered, linear and parallel to one other. The profiles are comparable to those of typical T-MORB series (Maury, 1993; Juteau

and Maury, 1999), for instance the moderately-enriched basalts from off-axis seamounts of the mid-Atlantic ridge (Le Roex et al., 1996, 2002). They do not show negative anomalies for Nb, Zr or Ti, which allows us to exclude a genesis in a supra-subduction context. The diabase dikes crosscutting the layered gabbros also show flat patterns and T-MORB type profiles, very similar to those of the extrusive sequence. The layered gabbros have cumulate compositions compatible with fractionation from N-MORB to T-MORB-type basaltic melts.

With these considerations in mind, we propose that the Late Cretaceous ophiolitic lavas of the Khoy region were formed at oceanic spreading centers by partial melting of a depleted mantle source, probably contaminated by one or several regional mantle plumes, that were responsible for the moderate enrichment in REE. The uniform patterns of their spectra suggest that there were no significant heterogeneities in the sources, as reported in the northern Atlantic, main fracture zones, and eastern Pacific. They do not show any depletion of HFSE (specially Ti, Nb and Zr) as reported in present-day arc-volcanics, and in 'supra-subduction' ophiolite complexes.

5.3. The most fractionated basalts are located at the base of the extrusive pile

These samples plot logically at the highest ordinates on the normalized multi-element plots. This suggests that the most evolved basalts were ponded at the roof of the magma chamber, and were extracted first. The basaltic flows that followed represent less evolved liquids, probably resulting from mixing events in the magma chamber with inputs of primitive magma.

At a smaller scale, the numerous alternations of phyric and aphyric basaltic flows along the studied sections suggest long residence times for the magma in the magma chamber, favouring the growth of plagioclase phenocrysts that then floated and accumulated at the roof of the magma chamber.

5.4. The Late Cretaceous ophiolite of Khoy was created along a slow-spreading oceanic ridge

In spite of the tectonics, our field geological studies have shown that the Khoy ophiolite consists of an extrusive sequence (mainly pillow lavas, often very phyric), resting directly over a plutonic sequence made of serpentinized lherzolites and harzburgites. The plutonic sequence contains intrusive bodies of layered gabbros, hectometric to kilometric in size. We did not find any trace of a diabasic sheeted dike complex in this ophiolite, which has all the characteristics of a slow-spreading oceanic ridge (mid-Atlantic ridge type).

According to recent studies of present-day oceanic crust, two main types of crustal organization can be defined (Juteau and Maury, 1999):

(a) Oceanic ridges with fast- to intermediate-spreading rates (>6 m/year), such as the east-Pacific rise, have a thick crust (6–8 km) and a continuous crustal structure. The crust includes a thin volcanic layer, a well developed diabasic sheeted dike complex (>1 km thick), and a several kilometers thick gabbroic layer, resting over a very depleted harzburgitic upper mantle (Francheteau et al., 1990, 1992). The seismic Moho discontinuity, in this case, corresponds to the gabbro-peridotite boundary. This structure is explained by the high frequency and volume of the magmatic activity along a fast-spreading oceanic ridge.

(b) Oceanic ridges with slow spreading rates ($<$ 6 cm/year), such as the mid-Atlantic ridge or the SW Indian ridge, form thin and discontinuous oceanic crust. A gabbroic layer as such does not exist, but resolves in numerous and small intrusive bodies (kilometer in size or less), intruding the residual upper mantle. A diabasic sheeted dike complex, although observed locally (Vema fracture zone: Auzende et al., 1988), is generally lacking (Auzende et al., 1994). The upper mantle is less depleted. This type of structural organization is explained by the low frequency and weak volume of magmatic activity at slow-spreading ridges, associated with intense tectonic activity favouring upwelling of the serpentinized upper mantle up to the ocean floor. In this case, the Moho seismic discontinuity would mark the lower boundary of the gabbroic pockets, and probably also that of the hydration (serpentinization) of the peridotite host-rocks (Cannat, 1993).

In the same manner, the structure of ophiolites may be classified into two types, identified both by their crustal organization and by the petrological nature of their residual mantle peridotites (Nicolas and Jackson, 1972; Nicolas, 1989; Juteau and Maury, 1999):

(a) Ophiolites with a thick and continuous crustal sequence, resting over a harzburgitic mantle sequence: this is the Harzburgitic Ophiolite Type or HOT, corresponding to what we know about fast-spreading oceanic ridges, and whose best example is the Oman ophiolite.

(b) Ophiolites showing a thin and discontinuous crustal sequence, with a Lherzolitic mantle sequence: this is the Lherzolitic Ophiolite Type or LOT, corresponding to slow-spreading oceanic ridges, and whose best example is the Ligurian–Piemont ophiolites, in the French-Italian Alps and Apennines (Elter, 1971; Decandia and Elter, 1972; Lemoine, 1980; Lagabrielle et al., 1984; Lagabrielle and Cannat, 1990).

According to these criteria, the Late Cretaceous ophiolite of Khoy presents clearly the characteristics of the LOT ophiolites, in particular:

- The residual mantle rocks are mainly composed of lherzolitesf and clinopyroxene-rich harzburgites, pointing to a 'LOT-type' residual mantle (Nicolas, 1989).
- The gabbros do not constitute a thick and continuous layer over the mantle rocks, but appear as small intrusive bodies inside the upper mantle.
- The submarine extrusives rest directly over the ultrabasic or gabbroic rocks, without any evidence of an intermediary sheeted dike complex of diabases.
- The volcanics are often extremely phyric.

The gabbroic intrusions present some surprising features. They are well layered, with a clear magmatic foliation, often affected by viscous deformations due to magmatic flow processes. On the other hand, they show a weak cryptic evolution of the mineral phases, and recurrent wehrlitic layers. These features suggest repeated inputs of primitive magma in the magma chamber, marked by the deposition of wehrlitic layers, thus preventing significant differentiation of the magma by crystal fractionation. These gabbroic intrusions may be compared to those described by Lagabrielle (1987) in the LOT ophiolites of the French–Italian Alps, which also show a dynamic layering and a variety of facies, ranging from ultramafic cumulates (wehrlites) to ferrogabbros. These 'gabbro pockets' however, show a continuous and regular evolution, from bottom to top, towards extremely evolved ferrogabbros without evidences of refeeding.

On slow-spreading ridges, as far as we know, layered gabbros are scarce, and magmatic evolutions are very fractionated (Dick et al., 1991). Coming back to the Khoy ophiolite, more detailed studies are needed to understand how the layering of the gabbros was created under such conditions. Clearly, the drag effect of the underlying flowing upper mantle on a mobile crystal mush cannot be invoked here, as in the Oman model (Boudier et al., 1996; Kelemen et al., 1997). Eventually, dynamic convective cells may have developed in these intrusions submitted to a high thermal gradient, making it easier to form layered cumulates.

5.5. The meta-ophiolites of Khoy probably also represent slow-spreading conditions

Although highly dismembered and tectonized, the meta-ophiolites included in the Eastern metamorphic complex of Khoy present some characteristics of the LOT ophiolites. The volcanic part, completely recrystallized to fine-grained amphibolites, is difficult to identify. We can only outline the fact that the fine-grained amphibolites of the m2 Unit show flat REE profiles of the T-Morb type, analogous to those of the extrusive sequence of the Late Cretaceous ophiolite.

The plutonic sequence preserved in these meta-ophiolites, however, has better resisted the metamorphic recrystallization, preserving the evidences of LOT organization: the peridotites are lherzolitic, and the metagabbros appear systematically as small-sized intrusions inside these peridotites, not as a continuous layer overlying them.

More detailed studies are here also necessary, but if these hypotheses were confirmed, this would mean that the oceanic basin which produced the ophiolites of Khoy was opening at a slow-spreading rate throughout all of Mesozoic time, not only during the Late Cretaceous.

Lastly, the splendid porphyroclastic to mylonitic tectonites preserved in these metamorphic slices attest extreme conditions of ductile shearing, met only in oceanic fracture zones either in present-day oceans (for instance in the St-Paul FZ, equatorial Atlantic: Hékinian et al., 2000), or in fossil FZ mapped in some ophiolite complexes (for instance in the Antalya ophiolite in Turkey: Reuber et al., 1884, or in the New-Caledonia ophiolite: Prinzhoffer and Nicolas, 1980).

5.6. The supra-ophiolitic series resting over the Late Cretaceous ophiolite constitutes a turbiditic sedimentary basin, fed by two volcanic sources

The supra-ophiolitic turbidites rework two main kinds of volcanic fragments: (a) basaltic fragments with typical T-MORB-type geochemistry, coming from the oceanic crust; (b) basaltic fragments with clear arc-type geochemistry (in particular Nb and Zr negative anomalies), coming from the Iran Block active margin.

We think that this turbiditic series accumulated in a subduction trench running along the northwestern margin of the Iran Block. The trench was fed with detrital volcanic fragments from both sides: T-MORB basalt fragments from the ocean-side, and arc-type basalts from the continent-side. The turbidites are overlain by volcanic breccias and flows of ankaramitic basalts, showing clear calc-alkaline affinities, followed above by pelagic sediments and pillow lava flows again made of T-MORB basalts.

It is important to note here that the extrusive sequence of the Late Cretaceous ophiolite is crosscut by late intrusive basaltic dikes, which are probably contemporaneous with the supra-ophiolitic turbiditic series. These late dikes have geochemical features indicating a 'supra-subduction' origin (with, in particular, the most pronounced Nb negative anomalies of all the analyzed lavas).

These data suggest that, during the Uppermost Cretaceous and Early Paleocene, the ocean floor corresponding to the ophiolite of Khoy was tectonically transferred to a 'supra-subduction' position. The supra-ophiolitic turbiditic series was therefore transferred to a back-arc basin environment, as suggested in our previous paper (Khalatbari-Jafari et al., 2004, Fig. 16).

6. Conclusion: geodynamic evolution of the Khoy area

The petrological and geochemical data presented in this paper are the indispensable complement of the field and geochronological data published last year in this same Journal (Khalatbari-Jafari et al., 2004).

They allow us to propose a reasonable scenario for the geodynamic evolution of the region of Khoy (see Khalatbari-Jafari et al., Fig. 16):

(1) After opening of the Neo-Tethys ocean during Late Permian, the Khoy oceanic basin developed by seafloor spreading.
(2) From Late Triassic to Late Cretaceous, the Khoy oceanic basin was simultaneously opening by seafloor-spreading, and subducting along its eastern margin beneath the Central Iran Block.
(3) The last oceanic lithosphere was produced during Late Cretaceous in a closing oceanic basin. This oceanic lithosphere was never subducted and remained unmetamorphosed, giving the Late Cretaceous ophiolite complex of Khoy. Volcanoclastic turbidites accumulated in the subduction trench, and unmetamorphosed igneous bodies (gabbros, granites) intruded the subduction metamorphic complex.
(4) Somewhat later (Early Paleocene), the western margin of the basin began to be underthrusted beneath the Late Cretaceous oceanic lithsophere, with production of late swarms of isolated calk–alkaline diabase dikes, cross-cutting the entire ophiolite of Khoy. Just before collision, the ophiolite of Khoy was obducted over the western metamorphic complex, probably representing a fragment of the Arabian–African shield.
(5) After collision and folding, calk–alkaline monzonitic subvolcanic intrusions (described in Khalatbari-Jafari et al., 2004) were intruded during Late Miocene in the Khoy ophiolite and its Paleocene–Eocene cover, leading to the present-day situation.

Acknowledgements

This study is the result of a PhD work (Khalatbari-Jafari, december 2002) defended at the Université de Bretagne Occidentale, Brest, France. It was carried out in the frame of a French–Iranian cooperative programme, supported by the French Ministry of Foreign Affairs, the Cultural Service of the French Embassy at Teheran, and the Geological Survey of Iran (GSI).

The authors want to thank M. Marcel Bohn for his precious help for the electron microprobe analyses (microprobe Camebax SX 50, Centre Ifremer de Brest), and Prof. Hervé Bellon for his constant help, support and constructive discussions.

References

Aghanabati, A., 2004. Major Sedimentary-structural Units of Iran. Geological Survey of Iran.

Arculus, J., 1994. Aspect of magma genesis in arcs. Lithos 33, 189–208.

Auzende, J.M., Bideau, D., Bonatti, E., Cannat, M., Honnorez, J., Lagabrielle, Y., Malavieille, J., Mamaloukas-Frangoulis, V., Mevel, C., 1988. Une coupe complète de la croûte océanique sur le mur Sud de la zone de fracture Vema (Atlantique central): résultats préliminaires de la campagne Vemanaute. C.R. Acad. Sci. Paris 307 (Ser. II), 2061–2067.

Auzende, J.M., Cannat, M., Gente, P., Henriet, J.P., Juteau, T., Karson, J., Lagabrielle, Y., Mevel, C., Tivey, M., 1994. Observation of sections of oceanic crust and mantle cropping out on the southern wall of Kane FZ. Terra Nova 6, 143–148.

Boudier, F., Nicolas, A., Ildefonse, B., 1996. Magma chambers in the Oman ophiolite: fed from the top and the bottom. Earth Planet. Sci. Lett. 144, 239–250.

Cannat, M., 1993. Emplacement of mantle rocks in the sea floor at mid-ocean edges. J. Geophys. Res., 98,4163-4172.

Coleman, R.G., 1986. Ophiolites and accretion of the North American Cordillera. Bull. Soc. Géol. France 8, 961–968.

Cotten, J., Le Dez, A., Bau, M., Maury, R.C., Dulski, P., Fourcade, S., Bohn, M., Brousse, R., 1995. Origin of anomalous rare-earth and yttrium enrichment in ubaerially exposed basalt: evidence from French polynesia. Chem. Geol. 119, 115–138.

DeBari, S.M., Coleman, R.G., 1989. Examination of the deep level of an island arc: evidence from Tonsna ultramafic_mafic assemblage, Tonsia, AK. J. Geophys. Res. 94, 4373–4391.

Decandia, A., Elter, P., 1972. La zona ofiolitifera del Bracco nel settore fra Levanto e la Val Graveglia (Apennino ligure). Mem. Soc. Geol. Ital. 11, 503–530.

Dick, H.J.B., Meyer, P.S., Bloomer, S., Kirby, S., Stakes, D., Mawer, C., 1991. Lithostratigraphic evolution of an in-situ section of oceanic layer 3. In: Von Herzen, R.P., Robinson, P.T. et al. (Eds.), Proceedings of ODP Science Results, College Station, pp. 439–537.

Elter, G., 1971. Schistes lustrés et ophiolites de la zone piémontaise entre Orco et Daire Baltée. Hypothèse sur l'origine des ophiolites. Géol. Alpine, Grenoble 47, 147–169.

Elthon, D., 1991. Geochemical evidence for formation of the Bay of Islands ophiolite above a subduction zone. Nature 354, 140–143.

Emami, M.H., Sadegi, M.M., Omrani, S.J., 1993. Magmatic Map of Iran, Scale 1/1,000,000. Geological Survey of Iran.

Francheteau, J., Armijo, R., Cheminée, J.L., Hékinian, R., Lonsdale, P., Blum, N., 1990. 1 Ma East Pacific Rise oceanic crust and uppermost mantle exposed by rifting in Hess Deep (equatorial Pacific Ocean). Earth Planet. Sci. Lett. 101, 281–295.

Francheteau, J., Armijo, R., Cheminée, J.L., Hékinian, R., Lonsdale, P., Blum, N., 1992. Dyke complex of the East Pacific Rise exposed in the walls of Hess Deep and the structure of the upper oceanic crust. Earth Planet. Sci. Lett. 111, 109–121.

Hawkins, J.W., Allen, J.F., 1994. Petrologic evolution of Lau Basin sites 834 through 839, Proceedings of ODP, Science Results, vol. 135, 1994 pp. 427–4780.

Hawkins, J.W., Melchior, J.T., 1985. Petrology of the Marizna Trough and Lau basin basalts. J. Geophys. Res. 90, 11431–11468.

Hékinian, R., Juteau, T., Gracia, E., Sichler, B., Sichel, S., Udintsev, G., Appriroual, R., Ligi, M., 2000. Submersible observations of Equatorial Atlantic mantle: the St. Paul fracture Zone region. Mar. Geophys. Res. 21, 529–660.

Hess, P., 1989. Origins of Igneous Rocks. Harvard University Press, Cambridge, MA. 336 pp.

Hofmann, A.W., 1988. Chemical diffrentiation of the earth: the relationship between mantle, continental crust, and oceanic crust. Earth Planet. Sci. Lett. 90, 297–314.

Humler, E., Whitechurch, H., 1988. Petrology of basalts from the central Indian Ridge (1at, 25° 23 S, long. 70°04 E): stimates of frequencies and fractional volumes of magma injections in a two-layered reservoir. Earth Planet. Sci. Lett. 88, 169–181.

Honnorez, S., Kirst, P., 1975. Submarine basaltic volcanism: morphometric parameters for discriminating hyaloclastites from hyalatuffs. Bull. Volcanol. 39–3, 1–25.

Hunter, R.H., 1996. Texture development in cumulate rocks, Layered Intrusions. Elsevier, Amsterdam.

Juteau, T., 2004. The ophiolites of Khoy (NW Iran): their significance in the Tethyan ophiolite belts of the Middle-East, Comptes Rendus Geoscience, vol. 336. Elsevier, Amsterdam pp. 105–108.

Juteau, T., Maury, R., 1999. The Oceanic Crust, from Accretion to Mantle Recycling, vol. 18. Springer, Chichester pp. 109–121.

Kelemen, P.B., Koga, K., Shimizu, N., 1997. Geochemistry of gabbro sills in the crust-mantle transition zone of the Oman ophiolite: implications for the origin of the oceanic lower crust. Earth Planet. Sci. Lett. 146, 475–488.

Khalatbari-Jafari, M., 2002. Etude géologique, pétro-géochimique et géochronologique des ophiolites de la région de Khoy (Iran). Thèse de doctorat (PhD), Université de Bretagne Occidentale, Brest, France, 252 p.

Khalatbari-Jafari, M., Juteau, T., Bellon, H., Emami, H., 2003. Discovery of two ophiolite complexes of different ages in the Khoy area (NW Iran), CR Geosciences, vol. 335. Académie des Sciences, Paris pp. 917–929.

Khalatbari-Jafari, M., Juteau, T., Bellon, H., Whitechurch, H., Cotten, J., Emami, H., 2004. New geological, geochronological and geochemical investigations on the Khoy ophiolites and related formations, NW Iran. J. Asian Earth Sci. 23, 507–535.

Lagabrielle, Y., 1987. Les ophiolites: marqueurs de l'histoire tectonique des domaines océaniques. Thèse Doctorat d'Etat, Univ. Bretagne Occidentale, Brest, 350 p.

Lagabrielle, Y., Cannat, M., 1990. Alpine jurassic ophiolites resemble the modern central Atlantic basement. Geology 18, 319–322.

Lagabrielle, Y., Polino, R., Auzende, J.M., Blanchet, R., Caby, R., Fudral, S., Lemoine, M., Mevel, C., Ohnenstetter, M., Robert, D., Tricart, P., 1984. Les témoins d'une tectonique intraocéanique dans le domaine téthysien: analyse des rapports entre les ophiolites et leurs couvertures métasédimentaires dans la zone piedmontaise des Alpes frano-italiennes. Ofioliti 9 (1), 67–88.

Le Bas, M.J., Le Maitre, R.W., Streckeisen, A., Zanettin, B., 1986. A chemical classification of volcanic rocks based on the total alkali-silica diagram. J. Petrol. 27, 745–750.

Lemoine, M., 1980. Serpentinites, gabbros and ophicalcites in the piemont-ligurian domain of the western Alps: possible indicators of oceanic fracture zones and associated serpentinite protrusions inthe jurassic-cretaceous Tethys. Arch. Sci., Geneva 33, 103–116.

Le Roex, A.P., Frey, F.A., Richardson, S.H., 1996. Petrogenesis of lavas from the AMAR valley and Narrowgate region of the FAMOUSvalley, 36°–37°N on the Mid-Atlantic Ridge. Contrib. Mineral. Petrol. 124, 167–184.

Le Roux, P.J., Le Roex, A.P., Schilling, J.G., 2002. Crystalisation processes beneath the southern Mid-Atlantic Ridge (45–55°s), evidence for high-pressure initiation of crystalisation. Contrib. Mineral. Petrol. 142, 582–602.

Maury, R.C., 1993. Les series volcaniques, Mém. Soc. géol. France, Pleins feux sur les volcans, vol. 163 1993 pp. 39–55.

McCulloch, M.T., Gamble, A.J., 1991. Geochemical and geodynamical constrations on subduction zone magmatism. Earth Planet. Sci. Lett. 102, 358–374.

Nelson, S.T., Montana, A., 1992. Sieve-textured plagioclase in volcanic rocks produced by rapid decompression, Amer. Mineral., 77, 1242-1249.

Nicolas, A., 1989. Structures of Ophjiolites and Dynamics of Oceanic Lithosphere. Kluwer Academic Publishers, Dordrecht. 367 p.

Nicolas, A., Jackson, E.D., 1972. Répartition en deux provinces des péridotites des chaînes alpines longeant la Méditerranée: implications géotectoniques. Bull. Suisse Minéral. Pétrol. 53, 385–401.

Niu, Y., Batiza, R., 1994. Magmatic processes at mid-Atlantic Ridge ~26°S. J. Geophys. Res. 99 (19), 719–19740.

Pallister, J.S., Hopson, C.A., Hopson, C.A., 1981. Samail ophiolite plutonic suite: field relation, phases variation, cryptic variation and layering, and a model of a spreading ridge magma chamber. J. Geophys. Res. 86, 2593–2644.

Parlak, O., Delaloye, M., Bingol, E., 1996. Phase and cryptic variation through the ultramafic-mafic cumulates in the Mersin ophiolite (southern Turkey). Ofioliti 21, 81–92.

Passchier, C.W., Trouw, R.A.J., 1995. Microtectonics. Springer, Berlin. 283 p.

Pearce, J.A., Cann, J.R., 1973. Tectonic setting of basic volcanic rocks determination using trace element analyses. Earth Planet. Sci. Lett. 69, 33–47.

Pearce, J.A., Norry, M.J., 1979. Petrogenetic implications of Ti, Zr, Y, and Nb, variation in volcanic rocks. Contib. Mineral. Petrol. 69, 33647.

Pearce, J.A., Lippard, S.J., Roberts, S., 1984. Characteristics and tectonic significance of supra-subduction zone ophiolites. In: Kokelaar, B.P., Howells, M.F. (Eds.), Marginal Basin Geology Geol. Soc. London Spec. Publ., 16, pp. 77–94.

Pefander, J.A., Jochum, K.P., Kozakov, I., 2002. Coupled evolution of back-arc and island arc-like mafic crust in the late-Neoproterozoic Agardagh Tes-Chem ophiolite, Central Asia: evidence from trace element and Sr–Nd–Pb isotope data. Contib. Mineral. Petrol. 143, 157–174.

Prinzhoffer, A., Nicolas, A., 1980. The Bogota Peninsula, New Caledonia: a possible oceanic transform fdault. J. Geol. 88, 387–397.

Reuber, I., Juteau, T., Whitechurch, H., 1984. Genèse en contexte transformant des ophiolites d'Antalya (Turquie). Bull. Soc. Géol. France (7) 26 (5), 945–954.

Ringwood, A.E., 1990. Slab-mantle interaction 3. Petrogenesis of intraplate magmas and the structure of the upper mantle. Chem. Geol. 82, 187–207.

Saunders, A., Tarnay, J., 1984. Geochemical characteristics of basaltic volcanism within back-arc basin. In: Kokelear, B.P., Howells, M.F. (Eds.), Marginal Basin Geology: Volcanic and Associated Sedimentary and Tectonic Processes in Modern and Ancient Marginal Bassins Geol. Soc. Spec. Pub. 16, pp. 59–76.

Shelley, D., 1993. Igneous and Metamorphic Rocks under the Microscope. Chapman & Hall, London. 445 p.

Shervais, J.W., 1982. The petrochemistry of ophiolite gabbroic complexes: a key for the classification of ophiolites into low-Ti and high-Ti types. Earth Planet. Sci. Lett. 52, 203–212.

Stakes, D.S., Shervais, J.W., Hopson, C.A., 1984. The Volcanic-Tectonic cycle of FAMOUS and AMAR valleys, Mid-Atlantic Ridge (36°47N): evidence from basalt glass and phenocryst compositional variation for a steady state magma chamber beneath the valley mid section, AMAR 3. J. Geophys. Res. 89, 6995–7028.

Stewart, M.L., Fowler, A.D., 2001. The nature and occurrence of discrete zoning in plagioclase from recently erupted andesitic volcanic rocks, Montserrat. J. Volcanol. Geotherm. Res. 106, 243–253.

Sun, S.S., Macdounough, W.F., 1989. Chemical and isotopic systematics of oceanic basalts: implications for mantle compositions and processes. In: Scannia, E., Nicolae, I., Tassinari, R. (Eds.), Tectono-magmatic Setting of the Jurassic Ophiolites from South Apuseni Mountains (Romania): Petrological and Geochemical Evidence Ofioliti, 26(1), pp. 9–22.